Spatial Statistics 65 (2025) 100869

Contents lists available at ScienceDirect

Spatial Statistics

journal homepage: www.elsevier.com/locate/spasta

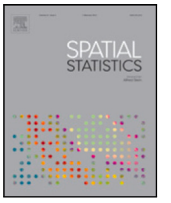

Pixel isotropy test based on directional perimeters

Mariem Abaach [a], Hermine Biermé [b], Elena Di Bernardino [c,*], Anne Estrade [a]

[a] Université Paris Cité, CNRS, UMR 8145, MAP5, Paris, France
[b] Université de Tours, CNRS, UMR 7013, IDP, France
[c] Université Côte d'Azur, CNRS UMR 7351, Laboratoire J.A. Dieudonné, France

ARTICLE INFO

Keywords:
Central limit theorem
Digital images
Discrete geometry
Isotropy test
Excursion sets
Gaussian random fields
Geometric statistics
Local counting algorithms
Medical imaging

ABSTRACT

In this paper we consider the so-called directional perimeters of a thresholded gray-level image. These geometrical quantities are built by considering separately the horizontal and vertical contributions of the pixel. We explicitly compute the first two moments of the directional perimeter under the hypothesis of an underlying discrete Gaussian stationary random field. We establish a central limit theorem (CLT), as the number of pixels goes to infinity, for the joint directional perimeters at various levels under a weak summability condition of the covariance function. By using the CLT previously established, we construct a consistent pixel isotropy test, based on the ratio of the directional perimeters. Our theoretical study is completed by extensive numerical illustrations based on simulated data. Finally, we apply our method to detect pixel anisotropy in calcaneus X-ray images.

Contents

* Corresponding author.
E-mail addresses: mariem.abaach@u-paris.fr (M. Abaach), hermine.bierme@univ-tours.fr (H. Biermé), elenadb@unice.fr (E. Di Bernardino), anne.estrade@u-paris.fr (A. Estrade).

https://doi.org/10.1016/j.spasta.2024.100869
Received 22 February 2024; Received in revised form 28 October 2024; Accepted 29 October 2024

Available online 20 November 2024

1. Introduction

1.1. Motivation and related literature

The main objective of our study is to be able to decide whether the texture of a gray-level image is isotropic or not. By the texture of an image, we mean the microscopic structure that is captured by the covariance function at the pixels scale. In order to achieve this goal, we propose a methodology built on a statistical test for which all steps are rigorously validated. The originality of our approach is to stick to the geometrical features of the image without trying to identify the full distribution of the underlying Gaussian random field that is supposed to serve as a model. More precisely, our observable statistic will be the perimeter of the black domain in the black and white image obtained through a thresholding procedure.

In the previous literature, a number of non-parametric tests of directional dependence have been developed using both the spatial and spectral representations of random fields (see, e.g., Weller and Hoeting, 2016; Guan et al., 2004). A comparative study with the Guan et al. (2004)'s method is proposed in Section 5. The statistical methodology of this paper is based on the well-known *local counting algorithms* (LCAs) that operate on individual pixels or small local neighborhoods and accumulate information locally (see, *e.g.*, Gray, 1971; Miller, 1999). The advantage of these algorithms is their simplicity, which allows for efficient implementation in parallel architecture (see, *e.g.*, Lindblad (2005)).

Although such type of statistical study of the excursion set (i.e., a region of the image where the pixel's values are higher than a fixed level) is an old engineers task (see Longuet-Higgins (1957) for instance), it has recently received much attention from a probability theory and mathematical statistics point of view. To cite some of these papers, let us quote Worsley (1996) or Telschow et al. (2020) where the localization of peaks is inferred from the observation of the Euler characteristic of excursion sets in neuroimaging and in the Cosmic Microwave Background radiation, Molina and Feito (2002) where isotropy is tested through the observation of the gradient, Di Bernardino et al. (2017) or Biermé et al. (2019) where a test of Gaussianity is produced based on the Euler characteristic of excursion sets, Abaach et al. (2021) where a test of symmetry of the marginal distribution of the field is produced based on the perimeter of thresholded images. Among this dense literature, let us focus on two specific works, Cabaña (1987) and Berzin (2021), with a similar objective as ours, namely a test of isotropy, based on the length of level sets. Both papers are concerned with affine two-dimensional continuous random fields, *i.e.* stationary random fields X defined on $\mathbb{R}^2$ and given as $X(\cdot) = Z(A\cdot)$, where Z is centered, stationary and isotropic defined on $\mathbb{R}^2$ and A is a deterministic matrix that can be reduced to $A = \begin{pmatrix} a & 0 \\ 0 & b \end{pmatrix} \begin{pmatrix} \cos\theta & \sin\theta \\ -\sin\theta & \cos\theta \end{pmatrix}$, $a, b \in \mathbb{R}$, $\theta \in [0, 2\pi)$. Within this continuous parametric frame, X is isotropic in distribution if and only if $a = b$. In both articles, a test of isotropy is constructed, based on the measurement of the respective horizontal and vertical components of the length of the level sets. In the former paper, some mixing conditions yields a Gaussian asymptotics of the normalized level set length, while in the latter article, a Gaussian condition yields a similar result. This central limit theorem is the crux for establishing a fair statistical test. Let us insist on the continuous setting that is assumed in those papers whereas our study definitively deals with discrete images. Our precise setting will be presented later on in the introductory section. Implementations of this type of "geometrical" methods can be found in medical imaging and image analysis in general, cosmology, hydrology, sea waves modeling, etc.

1.2. X-ray images of calcaneus bones

As an example, let us exhibit some medical images that can be handled with our methodology. In this introductory part, we just show the images and a first tentative of descriptive statistics. The statistical results that we are able to infer from our methodology is detailed in Section 6. We analyzed 211 X-ray images of calcaneus bones in order to detect the eventual anisotropic nature of the micro-architecture. Bone texture anisotropy is of special interest for the diagnosis of osteoporosis (see Chappard et al. (2005) for instance or Wani and Arora (2020) for a review). We first applied a preprocessing step in order to get stationary images and then consider the thresholded images at various empirical quantile levels t_α, *i.e.* for $\alpha \in (0, 1)$, there exists a proportion α of the image values smaller than t_α (see Fig. 1).

As observable statistics, we use the respective numbers of horizontal and vertical edges that separate a black pixel from a white pixel of the binary image obtained by truncation. We name these counters as directional perimeters, vertical and horizontal respectively (denoted below $\mathcal{P}^{(1)}$ and $\mathcal{P}^{(2)}$). In the case of an isotropic texture, the ratio of the two directional perimeters should be close to one. At the opposite, if the observed ratio is far from one, then some anisotropy is expected in the microscopic texture of the image. Remark that one could have the case that the image is anisotropic, but horizontal and vertical contributions of the perimeter are equal (see, for example, Fig. 13 for an illustration of this drawback). The ratio has been computed for each image at various empirical quantile levels t_α. In Fig. 2, the distribution of the obtained ratios is summarized in a boxplot for each considered value of α.

As it will be noticed in Proposition 3.1 (see in particular, Eqs. (3) and (5)), in a grid with small resolution (i.e., pixels correlation near to one), the ratio of the two directional perimeters is expected to be invariant in regard to the threshold. This invariant property

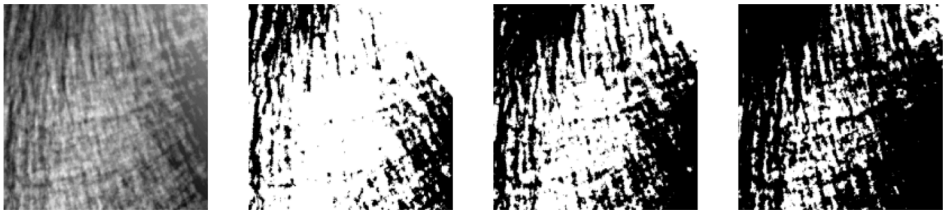

Fig. 1. Preprocessed bone X-ray image, with its associated excursion sets thresholded at the first, second and third quartiles.

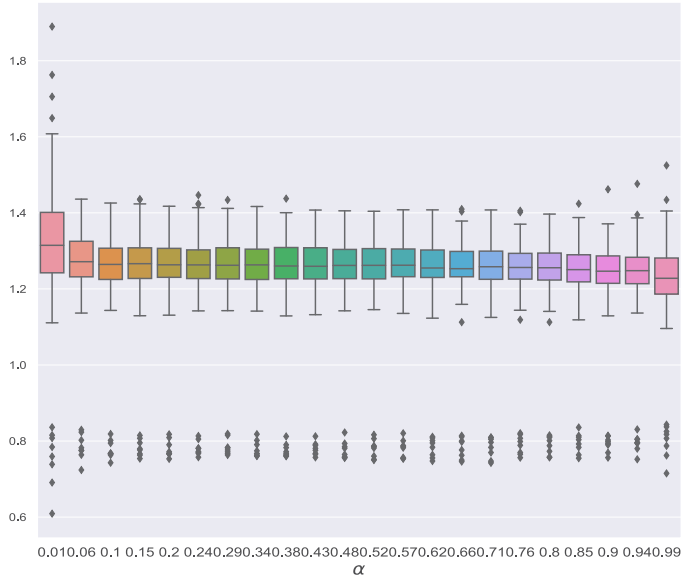

Fig. 2. Boxplots of the ratio between the two directional perimeters $\mathcal{P}^{(1)}(t_\alpha), \mathcal{P}^{(2)}(t_\alpha)$, computed at t_α quantile levels, for $\alpha \in [0.01, 0.99]$. Considered images: 211 stationary thresholded images of bone X-rays.

can be appreciated in Fig. 2 for the considered images of bone X-rays. Interestingly, this means that the anisotropy of the considered texture can be revealed at any threshold level by simply comparing two single counters. In Fig. 2, we observe that the boxplots of the ratio between the horizontal and vertical perimeters are not distributed around one. Moreover, for almost all images the observed ratios are above one whereas for some images extreme values are observed below one (for further details see Section 6). With a very different approach based on quadratic variations, the same sample of images has been analyzed in Biermé et al. (2009) and the same conclusion has been obtained: the calcaneus X-ray images are anisotropic. Specifically, the vertical and horizontal textures of the considered images are clearly differently organized. In Richard (2016), the investigation of the anisotropy property of textures was applied to medical images, in combination with a measure of texture roughness, as a means of detecting lesions in mammograms.

1.3. The proposed methodology and organization of the paper

Section 2 is devoted to the presentation of the considered mathematical framework. Assuming that the original gray-level image is a discrete Gaussian stationary field, we are able to explicitly compute the first two moments of the so-called directional perimeter (see Section 3). Our study of moments includes the asymptotic behavior as the number of pixels goes to infinity. We then establish a central limit theorem (CLT) (see Theorem 3.4) for the joint directional perimeters at various levels under a summability condition of the covariance function.

The next step consists in building the promised statistical test. More precisely, ρ being the covariance function of the Gaussian field and (e_1, e_2) being the canonical basis of $\mathbb{R}^2$, we consider the null hypothesis H_0: $\rho(e_1) = \rho(e_2)$ that we call "pixel isotropy" through a misuse of language. Then, we focus exclusively in the horizontal and vertical directions. We exhibit a statistic depending on the ratio of the directional perimeters that goes to one under H_0 thanks to the CLT previously established. Moreover, we prove the consistency of the proposed test. Let us insist on the fact that our test is a non-parametric one so that the alternative hypothesis reduces to H_1: $\rho(e_1) \neq \rho(e_2)$. Notice that these discrete perimeters on preferential axes (e_1, e_2) count the white–black and black–white transitions, i.e., the horizontal and vertical crossing numbers of the thresholded image. The theoretical study is completed by extensive numerical illustrations based on simulated data (see Section 4). We sample Gaussian fields with compact support covariances and use affine deformations to get anisotropic models. The performances of our test are illustrated on those models.

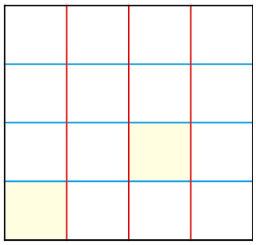

Fig. 3. Square tiling for $m = 4$. Two cells are represented in yellow, located at $(0,0)$ and at $(2,1)$. Vertical edges are in red and the horizontal ones in blue. (For interpretation of the references to color in this figure legend, the reader is referred to the web version of this article.)

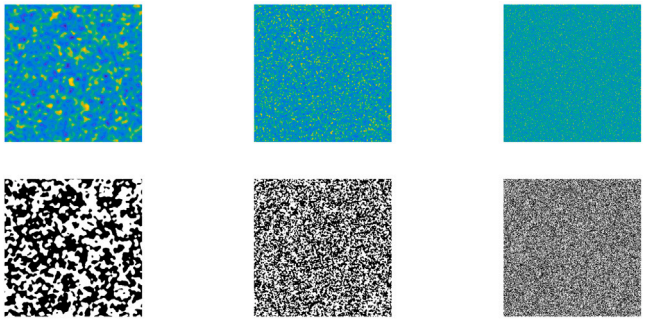

Fig. 4. Generations of Gaussian random fields with covariance $\rho(x) = e^{-\kappa\|x\|^2}$ (first row) and respective thresholded images $Z_m^{(t)}$, for $t = 0$ and $m = 512$ (second row). Considered values for κ: $0.01, 0.1, 1$ (from left to right).

The crucial question of estimating the variance of the perimeter is also explored. In Section 5 we propose a comparison in terms of obtained p_{values} with the semivariogram based isotropy test proposed by Guan et al. (2004). Finally, we apply our method to the calcaneus X-ray images that we have already presented in Section 6. It allows us to infer properties and to estimate quantities that could be of interest from a medical point of view. We end the paper by a concluding Section 7. We provide some supplementary lemmas that are used in the computation of the second moment of the directional perimeter and in the numerical computations (see Appendix A) as well as the proofs of the results and theorems presented in the paper (see Appendix B).

2. Mathematical framework

2.1. Construction of the binary image

Let m be an integer with $m \geq 2$. Without loss of generality, we consider our observation window as the square $S = [0, m]^2$ and we divide it into m^2 pairwise disjoint unit squares that we call cells. We consider the following set of points

$$\mathbb{G}_m := \{0, 1, \dots, m-1\}^2,$$

and we label each cell of S by its lower left corner, which corresponds to each point of $\mathbb{G}_m$. We denote by e_1, e_2 the elements of the canonical basis of $\mathbb{R}^2$. We call horizontal, respectively vertical, edge the segment from x to $x + e_1$, respectively from x to $x + e_2$, for any point in $\mathbb{G}_m$. Fig. 3 shows an example of a square tiling with $m = 4$.

Using this square tiling, we observe $(X_x)_{x\in\mathbb{G}_m}$, which we assume coincides with values of a stationary Gaussian random field $(X_x)_{x\in\mathbb{Z}^2}$ with unit variance, which means the correlation and covariance coincide. The stationarity hypothesis means that for all $h \in \mathbb{Z}^2$,

$$\left(X_{x+h}; x \in \mathbb{Z}^2\right) \overset{fdd}{=} \left(X_x; x \in \mathbb{Z}^2\right),$$

where fdd denotes finite-dimensional distributions. We denote by

$$\rho(x) := \text{Cov}\left(X_0, X_x\right),\ x \in \mathbb{Z}^2,$$

the covariance function of X.

Considering a threshold parameter $t \in \mathbb{R}$, we introduce the associated binary image $Z_m^{(t)} = \left(\mathbb{1}_{\{X_x \geq t\}}\right)_{x\in\mathbb{G}_m}$ where the cell located at x is associated to black or white according to whether $X_x \geq t$ or $X_x < t$. In Fig. 4 we display several random generations of Gaussian random fields and their associated thresholded images. Sampling is provided by using the Matlab function `stationary_Gaussian_process` (MATLAB, 2021).

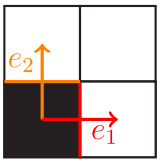

Fig. 5. Horizontal edge in orange, vertical one in red, contributing to the perimeter which is equal to 2. (For interpretation of the references to color in this figure legend, the reader is referred to the web version of this article.)

2.2. Directional perimeters of a binary image

Following the approach presented in Biermé and Desolneux (2021), for each edge we aim to know whether it contributes to the perimeter of the black component of $Z_m^{(t)}$ (see Fig. 5). Making use of the additive nature of the perimeter, one can start by computing the directional perimeter given each direction, horizontal and vertical.

Following this consideration, we introduce the next notation,

$$\mathbb{G}_m^{(1)} := \{0,1,\dots,m-2\} \times \{0,1,\dots,m-1\},$$
$$\mathbb{G}_m^{(2)} := \{0,1,\dots,m-1\} \times \{0,1,\dots,m-2\},$$

and for $i \in \{1,2\}$ we define the random quantity,

$$\begin{aligned} f_t^{(i)}(x) :=& \mathbb{1}_{\left\{\min\left(X_x, X_{x+e_i}\right) < t \le \max\left(X_x, X_{x+e_i}\right)\right\}}, \qquad x \in \mathbb{G}_m^{(i)}, \\ =& \mathbb{1}_{\{X_x < t\}} \mathbb{1}_{\{X_{x+e_i} \ge t\}} + \mathbb{1}_{\{X_x \ge t\}} \mathbb{1}_{\{X_{x+e_i} < t\}}, \end{aligned} \tag{1}$$

which takes into account the possible contribution of the edge between the cell located at x and the one located at $x + e_i$ to the perimeter of the black component of $Z_m^{(t)}$.

Let us now introduce the main tool of the present work.

Definition 2.1 (*Directional Perimeter of a Binary Image* $Z_m^{(t)}$). For $t \in \mathbb{R}$, we denote by $\mathcal{P}_m^{(i)}(t)$ the sum of all contributions over the ith direction (vertical for $i = 1$ and horizontal for $i = 2$) and we call it the directional perimeter of the binary image $Z_m^{(t)}$

$$\mathcal{P}_m^{(i)}(t) = \sum_{x \in \mathbb{G}_m^{(i)}} f_t^{(i)}(x). \tag{2}$$

The perimeter of $Z_m^{(t)}$ is given by $\mathcal{P}_m(t) := \mathcal{P}_m^{(1)}(t) + \mathcal{P}_m^{(2)}(t)$.

3. Statistics of the directional perimeter

3.1. First moment

Let us start by investigating the first moment of the directional perimeter $\mathcal{P}_m^{(i)}(t)$. The study of the second moment is postponed to Section 3.3.

In the next proposition, we give two closed formulas for the expected directional perimeter. The first one (see Eq. (3)) has an integral expression and uses the fact that the expectation of $f_t^{(i)}(x)$ is nothing but the probability of a crossing at level t. It can be found in Lantuéjoul (2002), Prop. 16.1.1, for instance. The second one (see Eq. (4)) suggests a numerical strategy to evaluate this integral, it will be widely used in the numerical studies in Section 4.

Proposition 3.1 (*First Moment of the Directional Perimeter*). *We assume that* $\left(X_x\right)_{x \in \mathbb{Z}^2}$ *is a stationary Gaussian centered with unit variance random field. Let* $i \in \{1,2\}$ *and let us denote by* $\rho(e_i) = \mathrm{Cov}\left(X_0, X_{e_i}\right) \in [-1,1]$. *Let* $t \in \mathbb{R}$, *then the expected value of the directional perimeter in (2) is given by*

$$\mathbb{E}\left(\mathcal{P}_m^{(i)}(t)\right) = m(m-1)\mathbb{E}\left(f_t^{(i)}(0)\right) = m(m-1)h(t,\rho(e_i)),$$

where

$$h(t,\rho(e_i)) = \int_{\rho(e_i)}^{1} \frac{\exp(-t^2/(1+u))}{\pi\sqrt{(1-u^2)}}\, du. \tag{3}$$

Moreover, if $\rho(e_i) \neq -1$,

$$\begin{aligned} &h(t,\rho(e_i)) \\ &= \mathbb{E}\left(\Phi\left(\frac{\sqrt{2}t + \sqrt{1-\rho(e_i)}\,|N|}{\sqrt{1+\rho(e_i)}}\right) - \Phi\left(\frac{\sqrt{2}t - \sqrt{1-\rho(e_i)}\,|N|}{\sqrt{1+\rho(e_i)}}\right)\right), \end{aligned} \tag{4}$$

with $N \sim \mathcal{N}(0,1)$ and Φ being the cumulative distribution function of the standard Gaussian.

The proof of Proposition 3.1 is postponed to Appendix B.

Let us emphasize that Eq. (3) yields

$$h(t,\rho(e_i)) \underset{\rho(e_i)\to 1^-}{\sim} \frac{\sqrt{1-\rho(e_i)}}{\pi\sqrt{2}} \exp(-t^2/2). \tag{5}$$

In particular, this situation occurs, assuming to observe the discretization of a continuous Gaussian field Y on a grid of small resolution $\varepsilon > 0$ such that $X(x) = Y(\varepsilon x)$, $x \in \mathbb{Z}^2$ since in this case $1-\rho(e_i) = \frac{1}{2}\mathrm{Var}(Y(\varepsilon e_i) - Y(0)) \underset{\varepsilon\to 0}{\to} 0$. Then Proposition 3.1 extends the corresponding result of Theorem 3.2 in Biermé and Desolneux (2021) where the asymptotic behavior for $\varepsilon \to 0$ is computed in the case of positively correlated Gaussian field. Note also that, in this setting, the ratio $\mathbb{E}\left(\mathcal{P}_m^{(1)}(t)\right)/\mathbb{E}\left(\mathcal{P}_m^{(2)}(t)\right)$ is therefore invariant with respect to $t \in \mathbb{R}$.

Remark 1 (*Degenerate Dependence Cases*)**.**

- In the case of a fully dependent field, *i.e* $\rho(e_i) = 1$, then $\mathbb{E}\left(\mathcal{P}_m^{(i)}(t)\right) = 0$.
- In the independent case, *i.e.* $\rho(e_i) = \mathrm{Cov}\left(X_0, X_{e_i}\right) = 0$, from Eq. (4), we can write,

$$\begin{aligned}\mathbb{E}\left(\mathcal{P}_m^{(i)}(t)\right) &= m(m-1)\mathbb{E}\left(\Phi\left(\sqrt{2}\,t + |N|\right) - \Phi\left(\sqrt{2}\,t - |N|\right)\right)\\ &= 2m(m-1)\Phi(t)\left(1-\Phi(t)\right).\end{aligned}$$

In this *i.i.d.* setting, we recover the same result as in Abaach et al. (2021) (see Proposition 3.1).

Integrating $\mathbb{E}(\mathcal{P}_m^{(i)}(t))$ along t in $\mathbb{R}$ with function h given by Eq. (3) and using Fubini–Tonelli Theorem, we deduce the next corollary.

Corollary 3.2. *Under the same assumptions as in Proposition 3.1, it holds that, for $i \in \{1,2\}$,*

$$\int_{\mathbb{R}} \mathbb{E}\left(\mathcal{P}_m^{(i)}(t)\right) dt = \frac{2m(m-1)}{\sqrt{\pi}}\left(\sqrt{1-\rho(e_i)}\right).$$

This result may actually be seen as a discrete analogous of co-area formula that links total variation with the perimeter of the excursion set. Actually, writing $f_t^{(i)}(x) = \mathbb{1}_{\{X_x < t \le X_{x+e_i}\}} + \mathbb{1}_{\{X_{x+e_i} < t \le X_x\}}$, one has simply

$$\int_{\mathbb{R}} f_t^{(i)}(x)dt = |X(x+e_i) - X(x)| \text{ and } \int_{\mathbb{R}} \mathcal{P}_m^{(i)}(t)dt = \sum_{x\in\mathbb{G}_m^{(i)}} |X(x+e_i) - X(x)|.$$

Then, that the total variation of the image is given by

$$\mathrm{TV}(X) := \sum_{i=1}^{2}\sum_{x\in\mathbb{G}_m^{(i)}} |X(x+e_i) - X(x)| = \sum_{i=1}^{2}\int_{\mathbb{R}} \mathcal{P}_m^{(i)}(t)dt.$$

Corollary 3.2 provides a simple expression for the first moment of the total variation and links it directly to $\rho(e_i)$, i.e., the covariance evaluated in the ith direction. Note that it can be used as an estimator for $\rho(e_i)$ (see Section 6).

Let us now remark that, for all $t \in \mathbb{R}$, the map $c \mapsto h(t,c)$ introduced in Proposition 3.1, Eq. (3) is decreasing on $(-1,1)$. It follows that the corresponding result holds for the expected directional perimeter.

Corollary 3.3. *Under the same assumptions as in Proposition 3.1, it holds that, for $i \neq j$ in $\{1,2\}$,*

if $\rho(e_i) < \rho(e_j)$ *then* $\mathbb{E}\left(\mathcal{P}_m^{(i)}(t)\right) > \mathbb{E}\left(\mathcal{P}_m^{(j)}(t)\right),\ \forall t \in \mathbb{R}.$

If moreover, $(Y_x)_{x\in\mathbb{Z}^2}$ is an other stationary, unit variance, Gaussian random field with covariance function ρ_Y and directional perimeter $\mathcal{P}_{Y,m}^{(i)}$

if $\rho(e_i) < \rho_Y(e_i)$ *then* $\mathbb{E}\left(\mathcal{P}_m^{(i)}(t)\right) > \mathbb{E}\left(\mathcal{P}_{Y,m}^{(i)}(t)\right),\ \forall t \in \mathbb{R}.$

Rephrasing Corollary 3.3, $\mathbb{E}\left(\mathcal{P}_m^{(1)}(t)\right) \neq \mathbb{E}\left(\mathcal{P}_m^{(2)}(t)\right)$ if and only if $\rho(e_1) \neq \rho(e_2)$. Now, assuming that the field X is isotropic, one consequence would be that $\rho(e_1) = \rho(e_2)$, which is equivalent to $\mathbb{E}\left(\mathcal{P}_m^{(1)}(t)\right)/\mathbb{E}\left(\mathcal{P}_m^{(2)}(t)\right) = 1$. Hence, in the case of isotropy, the ratio $\mathcal{P}_m^{(1)}(t)/\mathcal{P}_m^{(2)}(t)$ would be distributed around 1. This consideration will be crucial for the proposed pixel isotropy testing procedure that we discuss later in Section 3.2.

3.2. Pixel isotropy test using the directional perimeters

In order to construct a pixel isotropy test using the directional perimeters of the binary image, we first establish a central limit theorem for the variables $(\mathcal{P}_m^{(i)}(t))_m$ as m goes to infinity. To do that, we add some assumptions on the covariance function ρ of the field X.

$(\mathcal{A}1)$ $\lim_{m\to\infty} m^{-2} \sum_{x,y\in\mathbb{G}_m} \rho(x-y+h)$ exists $\forall\, h \in \{0, e_i, e_j, e_i - e_j; 1 \le i,j \le 2\}$.

$(\mathcal{A}2)$ $\lim_{m\to\infty} m^{-1} \sum_{k,l=0} \rho((k-l)e_i + \varepsilon e_j)$ exists $\forall\, \{i,j\} = \{1,2\}$ and $\varepsilon \in \{0,1\}$.

$(\mathcal{A}3)$ $\lim_{m\to\infty} m^{-2} \sum_{x,y\in\mathbb{G}_m} \rho(x-y)^2$ exists.

Note that if $\sum_{x\in\mathbb{Z}^2} |\rho(x)| < \infty$ then it also fulfills the three Assumptions $(\mathcal{A}1)$, $(\mathcal{A}2)$ and $(\mathcal{A}3)$.

Theorem 3.4 (*Multi-directional multivariate CLT for r-thresholds*). *We consider that $(X_x)_{x\in\mathbb{Z}^2}$ is a stationary standard Gaussian field with a covariance function that satisfies $(\mathcal{A}1)$, $(\mathcal{A}2)$ and $(\mathcal{A}3)$. Let r be a positive integer and $t_1, \dots, t_r \in \mathbb{R}$. Then,*

$$\frac{1}{m}\left(\begin{pmatrix} \mathcal{P}_m^{(1)}(t_1) \\ \vdots \\ \mathcal{P}_m^{(1)}(t_r) \\ \mathcal{P}_m^{(2)}(t_1) \\ \vdots \\ \mathcal{P}_m^{(2)}(t_r) \end{pmatrix} - \begin{pmatrix} \mathbb{E}(\mathcal{P}_m^{(1)}(t_1)) \\ \vdots \\ \mathbb{E}(\mathcal{P}_m^{(1)}(t_r)) \\ \mathbb{E}(\mathcal{P}_m^{(2)}(t_1)) \\ \vdots \\ \mathbb{E}(\mathcal{P}_m^{(2)}(t_r)) \end{pmatrix}\right) \xrightarrow[m\to\infty]{d} \mathcal{N}\left(0,\ \Sigma_{2r}^{\star}\right),$$

where $\xrightarrow{d}$ stands for the convergence in distribution and $\mathcal{N}\left(0,\ \Sigma_{2r}^{\star}\right)$ for the $2r$-dimensional centered Gaussian distribution with covariance matrix $\Sigma_{2r}^{\star}$ given by

$$\Sigma_{2r}^{\star}(l,i,k,j) := \lim_{m\to\infty} \mathrm{Cov}\left(\frac{1}{m}\mathcal{P}_m^{(i)}(t_l), \frac{1}{m}\mathcal{P}_m^{(j)}(t_k)\right), \tag{6}$$

for $i,j \in \{1,2\}$ and $k,l \in \{1,\dots,r\}$.

The proof of Theorem 3.4 is postponed to Appendix B. It is based on a convergence theorem formulated by Arcones (1994).

We now aim to build a test using the specific structure of the mean directional perimeter. Let us consider the null hypothesis, called below pixel isotropy,

$$H_0 \ : \ \rho(e_1) = \rho(e_2).$$

Under H_0, we remark that $\mathbb{E}\left(\mathcal{P}_m^{(1)}(t)\right) = \mathbb{E}\left(\mathcal{P}_m^{(2)}(t)\right)$ for all t. Making use of Theorem 3.4 for the Δ-method, we first need to introduce the scaled perimeters defined as $\widetilde{\mathcal{P}}_m^{(i)}(t) = \mathcal{P}_m^{(i)}(t)/(m(m-1))$ in such a way that we have now

$$m\left(\widetilde{\mathcal{P}}_m^{(i)}(t_l) - h(t_l, \rho(e_i))\right)_{1\le i\le 2, 1\le l\le r} \xrightarrow[m\to\infty]{d} \mathcal{N}\left(0,\ \Sigma_{2r}^{\star}\right),$$

with $h(t,\rho(e_i))$ defined in Eq. (3) in Proposition 3.1. Since $\mathcal{P}_m^{(1)}(t)/\mathcal{P}_m^{(2)}(t) = \widetilde{\mathcal{P}}_m^{(1)}(t)/\widetilde{\mathcal{P}}_m^{(2)}(t)$ and $\mathbb{E}(\mathcal{P}_m^{(1)}(t))/\mathbb{E}(\mathcal{P}_m^{(2)}(t)) = h(t,\rho(e_1))/h(t,\rho(e_2))$, we have the following Gaussian asymptotic result.

Proposition 3.5 (*CLT for the Ratio of Directional Perimeters*). *Let $t \in \mathbb{R}$ and $\mathcal{P}_m^{(i)}(t)$ be the directional perimeter over ith-direction ($i = 1,2$) introduced in Definition 2.1. Under the same assumptions as in Theorem 3.4, it holds that,*

$$m\left(\frac{\mathcal{P}_m^{(1)}(t)}{\mathcal{P}_m^{(2)}(t)} - \frac{\mathbb{E}\left(\mathcal{P}_m^{(1)}(t)\right)}{\mathbb{E}\left(\mathcal{P}_m^{(2)}(t)\right)}\right) \xrightarrow[m\to\infty]{d} \mathcal{N}\left(0, \widetilde{\sigma}^2(t)\right), \tag{7}$$

with $\widetilde{\sigma}^2(t) = (\sigma_{1,1}^{\star}(t)\mu_2(t)^2 - 2\mu_2(t)\mu_1(t)\sigma_{1,2}^{\star}(t) + \sigma_{2,2}^{\star}(t)\mu_1(t)^2)/\mu_2(t)^4$, $\mu_i(t) = h(t,\rho(e_i))$ as in (3) and $\sigma_{i,j}^{\star}(t) = \Sigma_2^{\star}(1,i,1,j)$ as in (6).

Furthermore, under H_0, it holds that

$$m\left(\frac{\mathcal{P}_m^{(1)}(t)}{\mathcal{P}_m^{(2)}(t)} - 1\right) \xrightarrow[m\to\infty]{d,H_0} \mathcal{N}\left(0, \widetilde{\sigma}_{H_0}^2(t)\right), \tag{8}$$

with $\widetilde{\sigma}_{H_0}^2(t) = (\sigma_{1,1}^{\star}(t) + \sigma_{2,2}^{\star}(t) - 2\sigma_{1,2}^{\star}(t))/\mu_2(t)^2$.

Taking advantage of Proposition 3.5, we base our pixel isotropy test on the following ratio,

$$R_m(t) = \frac{\mathcal{P}_m^{(1)}(t)}{\mathcal{P}_m^{(2)}(t)}.$$

Assuming that $\widetilde{\sigma}^2(t) > 0$ and considering a consistent empirical estimator $\widehat{\sigma}_m^2(t)$ of $\widetilde{\sigma}^2(t)$, then, from Proposition 3.5, it holds that

$$\frac{m}{\sqrt{\widehat{\sigma}_m^2(t)}}\left(R_m(t) - 1\right) \xrightarrow[m\to\infty]{d,H_0} \mathcal{N}(0,1).$$

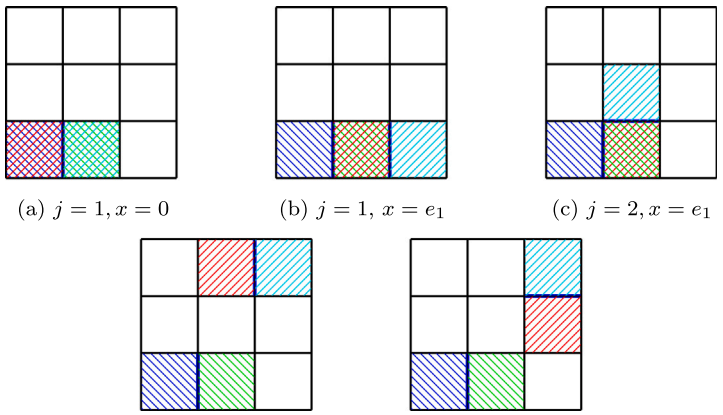

(a) $j = 1, x = 0$ (b) $j = 1,\ x = e_1$ (c) $j = 2, x = e_1$

(d) $j = 1, x = e_1 + 2e_2$ (e) $j = 2, x = 2e_1 + e_2$

Fig. 6. Illustration of the two-cells (case (a)), three-cells (case (b)–(c)) and four-cells (case (d)–(e)) configurations involved in the computation of $\mathrm{Cov}\left(f_t^{(1)}(0), f_s^{(j)}(x)\right)$.

Take a confidence level $\alpha \in (0,1)$ and set $q_{1-\frac{\alpha}{2}}$ such that $\mathbb{P}\left(|\mathcal{N}(0,1)| \leq q_{1-\frac{\alpha}{2}}\right) = 1 - \frac{\alpha}{2}$. We define the accessible test $\widehat{\phi}_m(t)$ with asymptotic level α as

$$\widehat{\phi}_m(t) = \mathbb{1}_{\left\{\frac{m}{\sqrt{\hat{\sigma}_m^2(t)}}|R_m(t)-1| \geq q_{1-\frac{\alpha}{2}}\right\}}. \tag{9}$$

Let us now raise the consistency question of the proposed test statistic under the alternative hypothesis $H_1 : \rho(e_1) \neq \rho(e_2)$. According to Corollary 3.3, if $\rho(e_1) \neq \rho(e_2)$ then $\mathbb{E}\left(\mathcal{P}_m^1(t)\right)/\mathbb{E}\left(\mathcal{P}_m^2(t)\right) \neq 1$, for all $t \in \mathbb{R}$. Hence, we have the following result.

Proposition 3.6 (*Consistency of the Proposed Isotropy Test*)**.** *For all $t \in \mathbb{R}$,*

$$\mathbb{P}_{H_1}\left(\widehat{\phi}_m(t) = 1\right) \to 1, \quad \textit{as} \quad m \to \infty.$$

Theorem 3.4 insures the existence of the asymptotic covariance of the directional perimeter but does not give any information regarding the explicit expression of the covariance in Eq. (6). The following section is devoted to this question.

3.3. Second moment

We now focus on the covariance function of the directional perimeters. Let us consider a stationary Gaussian random field $\left(X_x\right)_{x\in\mathbb{Z}^2}$ with zero mean and unit variance whose covariance structure is given by $\rho(x) = \mathrm{Cov}\left(X_0, X_x\right)$. Recalling that for a level $t \in \mathbb{R}$, a direction $i \in \{1,2\}$, one has by Eq. (2)

$$\mathcal{P}_m^{(i)}(t) = \sum_{x\in\mathbb{G}_m^{(i)}} f_t^{(i)}(x),$$

with $f_t^{(i)}(x)$ given by (1). For a level $s \in \mathbb{R}$ and a direction $j \in \{1,2\}$, the stationarity of X will allow to write $\mathrm{Cov}\left(\mathcal{P}_m^{(i)}(t), \mathcal{P}_m^{(j)}(s)\right)$ with respect to

$$\mathrm{Cov}\left(f_t^{(i)}(0), f_s^{(j)}(x)\right) = \mathbb{E}\left(f_t^{(i)}(0)\, f_s^{(j)}(x)\right) - \mathbb{E}\left(f_t^{(i)}(0)\right)\mathbb{E}\left(f_s^{(j)}(0)\right),$$

for some $x \in \mathbb{Z}^2$. The explicit expression of $\mathrm{Cov}\left(\mathcal{P}_m^{(i)}(t), \mathcal{P}_m^{(j)}(s)\right)$ in terms of $\mathrm{Cov}\left(f_t^{(i)}(0), f_s^{(j)}(x)\right)$ is postponed to Lemma A.4. Hence, getting the value of the directional perimeters covariances requires the computation of all the elements $\mathrm{Cov}\left(f_t^{(i)}(0), f_s^{(j)}(x)\right)$. Any of such elements has a two-, three- or four-cells structure, depending on the cardinality of the set $\{0, e_i, x, x+e_j\}$. For sake of simplicity let us fix $i = 1$. Fig. 6 shows the five types of configurations depending on the direction j and the position of x on the grid. Note that these configurations are generic ones. Indeed any possible configuration can be reduced to one of them by applying a single symmetry and/or a single translation. For this reason, in Lemma 3.7 below we focus our attention only on these typical configurations.

In view of Eq. (1), we make an observation that will appear very useful in the following: for any $a, b, t \in \mathbb{R}$,

$$\min(a,b) \leq t \leq \max(a,b) \iff |2t - (a+b)| \leq |b-a|.$$

Noting that for any $x \in \mathbb{G}_m^{(j)}$, we have $\mathbb{P}(X_x = X_{x+e_j}) = \mathbb{P}(X_0 = X_{e_j}) = 0$ as soon as $\rho(e_j) \neq 1$, we get

$$f_s^{(j)}(x) = \mathbb{1}_{\left\{\left|2s-(X_x+X_{x+e_j})\right| \leq \left|X_x - X_{x+e_j}\right|\right\}} \ a.s. \tag{10}$$

In order to compute $\mathbb{E}\left(f_t^{(1)}(0)\, f_s^{(j)}(x)\right)$, and using (10) when $|\rho(e_j)| \neq 1$ for $j \in \{1,2\}$, we introduce the following independent Gaussian variables,

$$\Delta_x^{(j)} := X_{x+e_j} - X_x \quad \text{and} \quad S_x^{(j)} := X_{x+e_j} + X_x. \tag{11}$$

Using these new variables, next lemma summarizes the way to compute $\mathbb{E}\left(f_t^{(1)}(0)\, f_s^{(j)}(x)\right)$ depending on the number of cells that are concerned.

Lemma 3.7. *With the notation (11), for $j \in \{1,2\}$,*

- *if $card\{0, e_1, x, x+e_j\} = 4$,*
$$\mathbb{E}\left(f_t^{(1)}(0)\, f_s^{(j)}(x)\right) = \mathbb{E}\left(\mathbb{1}_{\left\{|2t-S_0^{(1)}| \leq |\Delta_0^{(1)}|\right\}} \mathbb{1}_{\left\{|2s-S_x^{(j)}| \leq |\Delta_x^{(j)}|\right\}}\right);$$
- *if $card\{0, e_1, x, x+e_j\} = 3$ with $x = e_1$,*
$$\mathbb{E}\left(f_t^{(1)}(0)\, f_s^{(j)}(e_1)\right) = \mathbb{E}\left(\mathbb{1}_{\left\{|2t-S_0^{(1)}| \leq |\Delta_0^{(1)}|\right\}} \mathbb{1}_{\left\{|2s-(S_0^{(1)}+\Delta_0^{(1)}+\Delta_{e_1}^{(j)})| \leq |\Delta_{e_1}^{(j)}|\right\}}\right);$$
- *if $card\{0, e_1, x, x+e_j\} = 2$ with $x = 0$ and $j = 1$,*
$$\mathbb{E}\left(f_t^{(1)}(0)\, f_s^{(1)}(0)\right) = \mathbb{E}\left(\mathbb{1}_{\left\{|2t-S_0^{(1)}| \leq |\Delta_0^{(1)}|\right\}} \mathbb{1}_{\left\{|2s-S_0^{(1)}| \leq |\Delta_0^{(1)}|\right\}}\right).$$

Note that the covariance matrix of $(\Delta_0^{(1)}, S_0^{(1)}, \Delta_x^{(j)}, S_x^{(j)})$ has the same rank as the covariance matrix of $(X_0, X_{e_1}, X_x, X_{x+e_j})$ since the former Gaussian vector is obtained from the latter through an invertible linear transformation.

In Appendix A, we provide closed formulas for $\mathbb{E}\left(f_t^{(1)}(0)\, f_s^{(j)}(x)\right)$ in each of the three typical configurations that are mentioned in the above lemma (see Lemmas A.1–A.3). Such formulas can be obtained via a classical Gaussian regression. We actually do not use this formalism and prefer to write the considered projections with explicit coefficients. In this way we will be able to numerically approximate the theoretical covariance (see Section 4).

We now state a classical result that validates the fact that, under a mild assumption, the computation of 2-cells, 3-cells and 4-cells contributions, involves non-degenerate Gaussian vector whatever the configuration is. For a self-contained purpose, we give a proof of the next lemma in Appendix B.

Lemma 3.8. *Let $n \in \mathbb{Z}^+, n > 0$ and $\left(X_x\right)_{x\in\mathbb{Z}^2}$ be a stationary Gaussian random field and ρ its covariance function. Let us assume that ρ admits a spectral density. Then, if $x_1, \ldots, x_n$ are n distinct points in $\mathbb{Z}^2$, the covariance matrix Σ_n of the Gaussian vector $\left(X_{x_1}, \ldots, X_{x_n}\right)$, is invertible.*

In particular, in our setting, if ρ corresponds to a spectral measure that has a density we can state that the rank of the covariance matrix of $(X_0, X_{e_1}, X_x, X_{x+e_j})$ is equal to the cardinality of the set $\{0, e_1, x, x+e_j\}$.

These formulas also permit to exhibit an explicit upper bound for the covariance of the directional perimeter as stated in the next lemma.

Lemma 3.9. *Let $j \in \{1,2\}$ and let $x \in \mathbb{Z}^2$ such that the covariance matrix of the Gaussian vector $\left(X_0, X_{e_1}, X_x, X_{x+e_j}\right)$ is invertible and let us define*

$$r(x) = \max\left(|\rho(x)|, |\rho(x+e_j)|, |\rho(x-e_1)|, |\rho(x+e_j-e_1)|\right).$$

Then, there exists a constant $C \in \mathbb{R}^+$ that only depends on ρ such that, for any $s, t \in \mathbb{R}$ and any $x \in \mathbb{Z}^2$,

$$|Cov\left(f_t^{(1)}(0), f_s^{(j)}(x)\right)| \leq C r(x).$$

The proof of Lemma 3.9 is postponed to Appendix B. Note that this result allows to get a uniform bound on directional perimeters covariances, whatever directions or levels are chosen.

4. Numerical studies

The model we use to illustrate our theoretical results is a parametric model that belongs to the class of affine Gaussian processes with a covariance function with compact support, commonly known as m-dependent field. This model falls within the framework of the central limit Theorem 3.4. The parametric nature proves to be advantageous in the analysis of the behavior of the test under

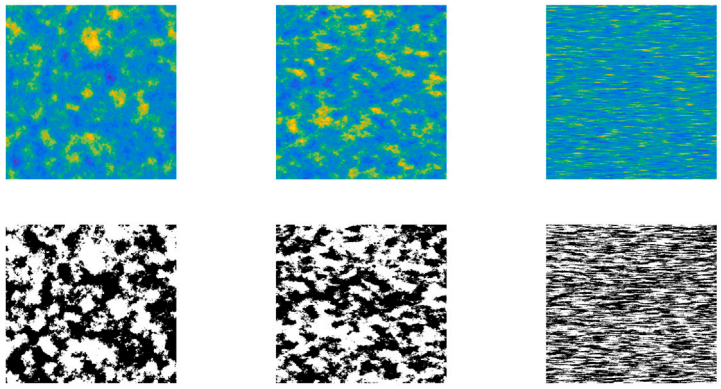

Fig. 7. Generations of affine Gaussian random fields with covariance as in (12) (first row) and respective thresholded images $Z_m^{(t)}$, for $t = 0$ and $m = 512$ (second row). Considered values for the parameter b: $1, 1.5, 10$ (from left to right).

the alternative hypothesis (H_1). Let $\{X(x; b, \theta, C); x \in \mathbb{Z}^2\}$, be a stationary centered unit variance Gaussian field with the so-called *spherical covariance* function (see Lantuéjoul (2002) or Bulinski et al. (2012)) given by

$$\rho(x) = (1 - 3\|Ax\|/2C + (\|Ax\|)^3/2C^3)\mathbb{1}_{\{\|Ax\| \le C\}}, \tag{12}$$

where

$$A := \begin{pmatrix} 1 & 0 \\ 0 & b \end{pmatrix} \begin{pmatrix} \cos(\theta) & \sin(\theta) \\ -\sin(\theta) & \cos(\theta) \end{pmatrix}$$

with $b \ge 1$, $\theta \in [0, \pi)$ and $C \ge 1$. Notice that covariance in (12) is not exactly "spherical" since it has been deformed by matrix A. Note also that it satisfies assumptions of Lemma 3.8. Initially, we choose to illustrate the computations of the statistics of the directional perimeter, using this covariance structure with $\theta = 0$, then we consider different values for θ.

In this section, for the sake of readability, we will note MCINT the number of Monte Carlo sample generations for the integral approximation of the closed formulas of the moments and n the number of Monte Carlo sample generations for the empirical estimation of the mean and the variance.

Section 4.1 (*resp.* Section 4.2) is devoted to validate first (*resp.* second) moment theoretical results and in Section 4.3 we illustrate the finite sample performances of the proposed pixel isotropy test. In Fig. 7 we display several random generations of affine Gaussian random fields with covariance as in (12) and their associated thresholded images. One can appreciate the impact of the b parameter on the anisotropy of the field. Sampling is provided by using the Matlab function `stationary_Gaussian_process` (see MATLAB (2021)).

4.1. Numerical studies of the expected directional perimeter

We start our numerical studies with the first moment (see Figs. 8 and 9 (left panel)). We compare the theoretical results obtained in Section 3.1 with the associated empirical counterparts. The empirical curves in Figs. 8 and 9 (left panel) are computed by simulating $n = 1\,000\,000$ Gaussian vectors of dimension 2 with the proper covariance structure and computing the expectation of the indicator function directly. The theoretical expectations in Figs. 8 and 9 (left panel) are numerically approximated with MCINT $= 1\,000\,000$.

Fig. 8 is a plot of the value of $\mathbb{E}\big(f_t^{(2)}(0)\big)$ for $t \in [-3, 3]$. We compare the theoretical curve in Proposition 3.1 with the empirical one for different values of the parameter b. In Fig. 8, one can appreciate the adequacy of the predicted theoretical values of $\mathbb{E}\big(f_t^{(2)}(0)\big)$ with respect to the estimated ones. Furthermore, these values increase with the anisotropy parameter b (see Fig. 8, from left to right panels). Fig. 9 (left panel) shows the evolution of $\mathbb{E}\big(f_0^{(2)}(0)\big)$, i.e., for the nodal level $t = 0$, in Proposition 3.1 as a function of b. As b grows, $\rho(e_2)$ goes to 0, converging towards an independent framework, which increases the length of the perimeter in the direction e_2 (see Fig. 9 (left panel)).

4.2. Numerical studies of the directional perimeter variances

By using the second moment theoretical study in Section 3.3, here we numerically evaluate the theoretical closed formulas contained in Lemmas A.1–A.3 for the second moment. Furthermore, we provide a comparison with their empirical counterparts. To this aim, we consider two approaches for the empirical estimation of variance $\widetilde{\sigma}^2(t)$ in Proposition 3.5.

The first approach relies on having n independent realizations of the random field $(X_x)_{x \in \mathbb{G}_m}$ (*i.e* n images of size m). We start by fixing the threshold level t and computing the ratio $(R_{m,i}(t))_{1 \le i \le n}$, for all n images. Then we consider the classical empirical estimator of the variance denoted here $\widehat{\sigma}^{(1)}_{n,m}(t)$. In the following we will refer to this method as *the Monte Carlo* method.

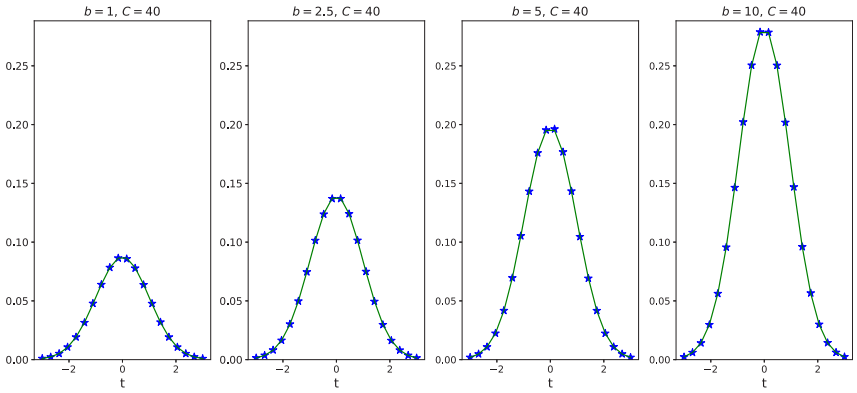

Fig. 8. $\mathbb{E}\big(f_t^{(2)}(0)\big)$ computed for different values of b as a function of t. Theoretical results in full green lines and the empirical estimated ones in blue stars. Here MCINT $= 1\,000\,000$ for the full green lines and $n = 1\,000\,000$ for the empirical blue stars. Different values of $b = 1, 2.5, 5, 10$ and $C = 40$.

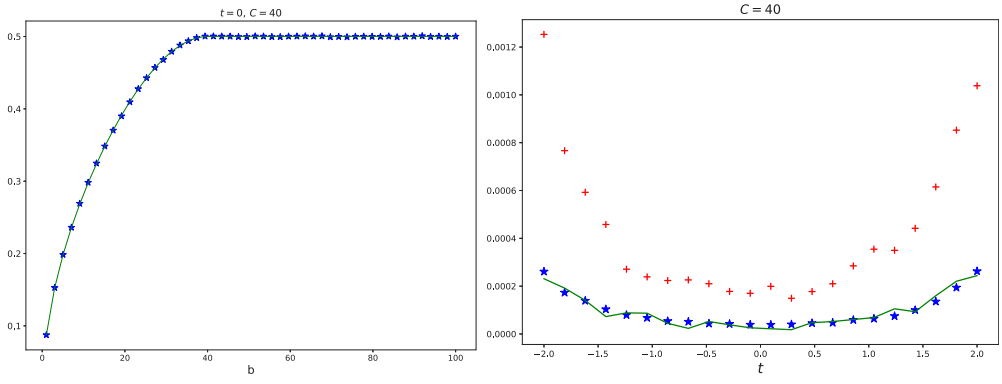

Fig. 9. Left panel: Theoretical $\mathbb{E}\big(f_0^{(2)}(0)\big)$ (full green lines); the empirical estimated ones (blue stars), as a function of b and with $C = 40$. Here MCINT $= 1\,000\,000$, $n = 1\,000\,000$. Right panel: Variances of the ratio of the directional perimeters for the Gaussian covariance model with angle $\theta = 0$, $C = 40$ and $b = 1$. Values of estimators $\widehat{\sigma}^{(1)}_{n,m}(t)$ (blue stars), $\widehat{\sigma}^{(2)}_{M_m,m}(t)$ (red crosses), theoretical associated values (full green line).

The second considered method is inspired by Di Bernardino and Duval (2022) and is referred to as the *sub-window* method. It consists in dividing the observation window S in $M_m \in \mathbb{N}$ patches, computing the ratio on each individual patch and computing the empirical variance, denoted here $\widehat{\sigma}^{(2)}_{M_m,m}(t)$. We compute this second estimator on distant domains, mimicking the classical context of *i.i.d.* random variables. This setting is used in Di Bernardino and Duval (2022) (Section 3.1.1) to establish the consistency of this variance estimator.

In Fig. 9 (right panel) we consider the Gaussian covariance model as in (12) for angle $\theta = 0$, $C = 40$ and $b = 1$. We display the values of the empirical variances of the ratio of the directional perimeters $\widehat{\sigma}^{(1)}_{n,m}(t)$ (blue stars) and $\widehat{\sigma}^{(2)}_{M_m,m}(t)$ (red crosses). To compute $\widehat{\sigma}^{(1)}_{n,m}(t)$ we use $n = 2000$ images of size $m = 512$ and for $\widehat{\sigma}^{(2)}_{M_m,m}(t)$, we used a unique image of size $m = 4800$ and the size of sub-patches $M_m = 240$. Furthermore in Fig. 9 (right panel), we represent the theoretical values of $\widetilde{\sigma}^2_{H_0}(t)$ (full green line) obtained in Proposition 3.5, via the integral numerical approximation with MCINT $= 1\,000\,000$. Fig. 9 (right panel) shows high adequacy between the empirical variances $\widehat{\sigma}^{(1)}_{n,m}(t)$ (blue stars) and the prescribed theoretical asymptotic variance values in Proposition 3.5. Unsurprisingly, a weaker performance is shown by the sub-window based estimator $\widehat{\sigma}^{(2)}_{M_m,m}(t)$ (red crosses).

Fig. 10, left panel, represents the theoretical variances (both panels, full green lines) of the perimeter $\mathrm{Var}\big(\frac{1}{m}\mathcal{P}_m(t)\big)$ in Lemma A.4 (see Eq. (A.3)) as a function of levels t, for $m = 512$ and different values of C. For the numerical approximation of the theoretical integrals, we consider MCINT $= 1\,000\,000$. In Fig. 10, left panel, we also display empirical variances computed via $\widehat{\sigma}^{(1)}_{n,m}(t)$ with $n = 2000$ and $m = 512$ (blue stars in both panels). In the obtained left panel of Fig. 10 we can analyze the behavior of variances with respect to the spatial dependence in the field. Recall that parameter C introduced in (12) is the length of the compact support of the covariance function ρ (*i.e.*, the bigger the value of C the longer the spatial dependence). We observe that the second moment of the perimeter is an increasing function of C and that the variance is maximal for the thresholds $t = -1$ and $t = 1$ and reaches a local minimum on the nodal level, $t = 0$. Finally, in the right panel of Fig. 10, we fix $C = 40$ and we add the empirical variances computed via $\widehat{\sigma}^{(2)}_{M_m,m}(t)$ with one single image of size $m = 4800$, patches size $M_m = 240$ (red crosses). The concordance between theoretical variance values and estimated ones can be appreciated.

Finally, notice that the nodal level $t = 0$ is the global maximum of the expected directional perimeter (see Fig. 8) and a local minimum of the variance (see Fig. 10), which makes it the optimal level to consider for inference purposes.

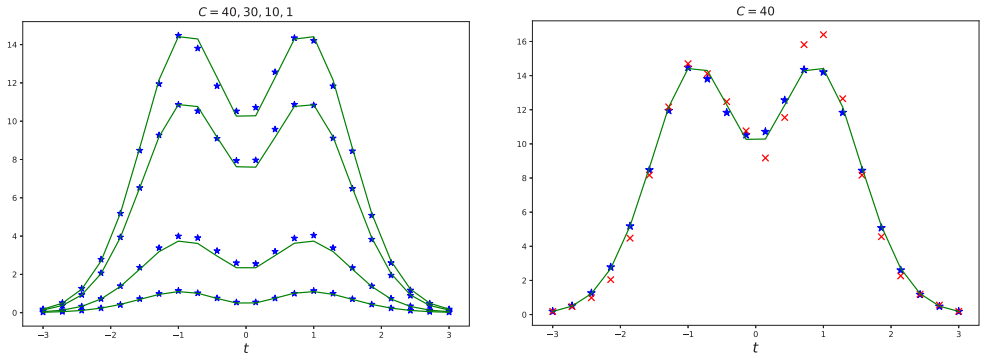

Fig. 10. Both panels: theoretical values of $\mathrm{Var}\big(\frac{1}{m}\mathcal{P}_m(t)\big)$, $m = 512$ (full green lines), empirical variance values $\widehat{\sigma}^{(1)}_{n,m}(t)$ (blue stars) with $n = 2000$. Left panel: $b = 1$ and from top to bottom $C = 40, 30, 10, 1$. Right panel: $b = 1$ and $C = 40$. Estimation of the variance by using the sub-window $\widehat{\sigma}^{(2)}_{M_m,m}(t)$ (red crosses). Here the image of size $m = 4800$ and the size of patches $M_m = 240$.

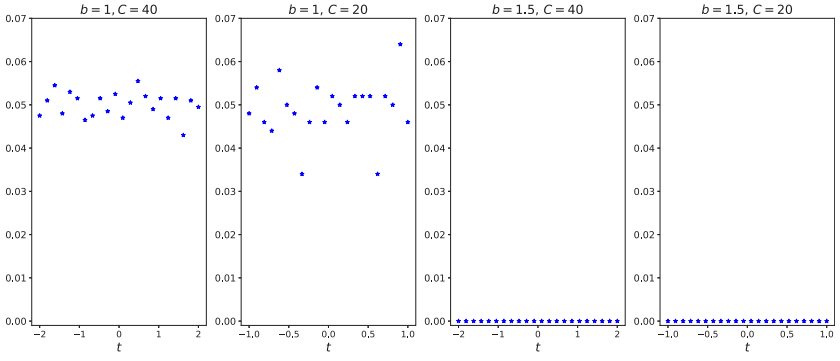

(a) Under H_0 : $\mathbb{P}_{H_0}(\widehat{\phi}_m(t) = 1)$ (b) Under H_1 : $\widehat{p}_{\text{value}}$

Fig. 11. Values of the empirical probability $\mathbb{P}_{H_0}(\widehat{\phi}_m(t) = 1)$ under H_0 with $b = 1$ (panel (a)) estimated on 100 repetitions and $\widehat{p}_{\text{value}}$ with $\widehat{\sigma}^2_m(t) = \widehat{\sigma}^{(1)}_{n,m}(t)$ under H_1 with $b = 1.5$ (panel (b)), as functions of levels t. First and third plots: $n = 2000$ images of size $m = 512$, $C = 40$ and $t \in [-2, 2]$. Second and fourth plots: $n = 500$ images of size $m = 512$, $C = 20$ and $t \in [-1, 1]$.

4.3. Numerical studies of pixel isotropy test

To illustrate the finite sample behavior of our pixel isotropy test, we choose two strategies.

(i) Computing the empirical probability on n samples,

$$\mathbb{P}_{H_0}(\widehat{\phi}_{m,i}(t) = 1), \text{ with } i = 1, \dots, n, \tag{13}$$

and $\widehat{\phi}_{m,i}(t) = \mathbb{1}_{\{m/\sqrt{\widehat{\sigma}^2_m(t)}\,|R_{m,i}(t)-1| \geq q_{1-\frac{\alpha}{2}}\}}$ with significance level $\alpha = 0.05$ (see Eq. (9)), where the ratio $R_{m,i}$ is empirically evaluated on generated samples.

(ii) Computing the p_{value}

$$\widehat{p}_{\text{value}} = \frac{1}{n}\sum_{i=1}^{n} 2\mathbb{P}\left(\mathcal{N}(0,1) \geq |z_i|\right) \text{ with } z_i = (R_{m,i}(t) - 1)/\sqrt{\widehat{\sigma}^2_m(t)}. \tag{14}$$

The variance $\widehat{\sigma}^2_m(t)$ in Eqs. (13) and (14) above is estimated via $\widehat{\sigma}^{(1)}_{n,m}(t)$ in Fig. 11 and via $\widehat{\sigma}^{(2)}_{M_m,m}(t)$ in Fig. 12.

In Fig. 11, we represent the empirical probability in Eq. (13) (panel (a)) and the $\widehat{p}_{\text{value}}$ in Eq. (14) with $\widehat{\sigma}^2_m(t) = \widehat{\sigma}^{(1)}_{n,m}(t)$ (panel (b)).

The Monte Carlo estimator variance is computed by considering for the first and third panels $n = 2000$ images of size $m = 512$, $C = 40$ and $t \in [-2, 2]$. For the second and fourth panels we consider $n = 500$ images of size $m = 512$, $C = 20$ and $t \in [-1, 1]$. Notice that in Fig. 11, the values of $\widehat{\mathbb{P}}_{H_0}(\widehat{\phi}_m(t) = 1)$ under H_0 range from 0.04 and 0.06 (panel (a)). Under H_1 (panel (b)) the average value of the p_{value} is $< 10^{-4}$.

Similarly to Fig. 11, in Fig. 12, we represent the empirical probability in Eq. (13) (panel (a)) and the $\widehat{p}_{\text{value}}$ in Eq. (14) with $\widehat{\sigma}^2_m(t) = \widehat{\sigma}^{(2)}_{M_m,m}(t)$ (panel (b)). This sub-window variance is computed by considering for the first and third plots, one single image of

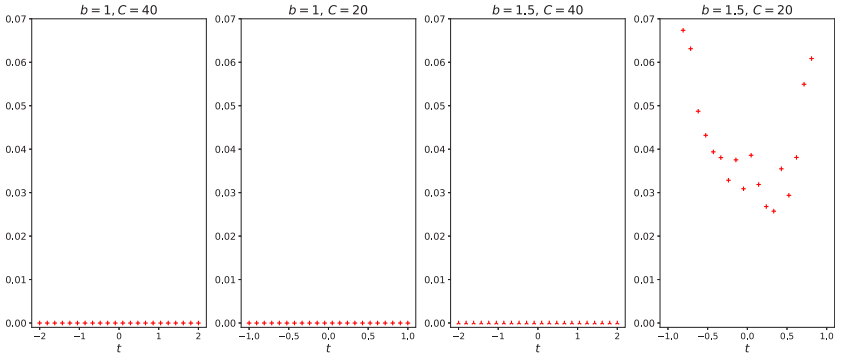

(a) Under H_0 : $\mathbb{P}_{H_0}(\widehat{\phi}_m(t) = 1)$ (b) Under H_1 : $\widehat{p}_{\text{value}}$

Fig. 12. Values of the empirical probability $\mathbb{P}_{H_0}(\widehat{\phi}_m(t) = 1)$ under H_0 with $b = 1$ (panel (a)) estimated on 100 repetitions and the $\widehat{p}_{\text{value}}$ with $\widehat{\sigma}^2_m(t) = \widehat{\sigma}^{(2)}_{M_m,m}(t)$ under H_1 with $b = 1.5$ (panel (b)), as functions of levels t. First and third plots: one single image of size $m = 4800$, $M_m = 240$, $C = 40$ and $t \in [-2, 2]$. Second and fourth panels: $m = 1024$, $M_m = 32$, $C = 20$ and $t \in [-1, 1]$.

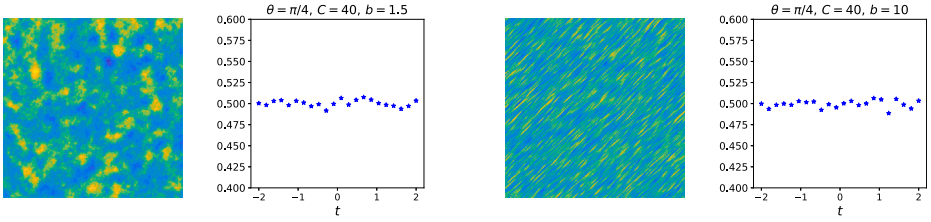

Fig. 13. Two generations of an affine Gaussian random field with the considered covariance of a compact support with $m = 512$, $\theta = \pi/4$, $C = 40$ and $b = 1.5$ (first panel) and $b = 10$ (third panel). $\widehat{p}_{\text{value}}$ with $\widehat{\sigma}^2_m(t) = \widehat{\sigma}^{(1)}_{n,m}(t)$ for $n = 2000$, $m = 512$.

Table 1
$\widehat{p}_{\text{value}}$ of the proposed test with $\widehat{\sigma}^2_m(t) = \widehat{\sigma}^{(1)}_{n,m}(t)$ by considering $n = 2000$ images of size $m = 512$.

b \ t	−2	−1	−0.5	0	0.2	0.5	1	2
1.1	0.04	$<10^{-4}$	$<10^{-4}$	$<10^{-4}$	$<10^{-4}$	$<10^{-4}$	$<10^{-4}$	0.04
1.2	0.0001	$<10^{-4}$	$<10^{-4}$	$<10^{-4}$	$<10^{-4}$	$<10^{-4}$	$<10^{-4}$	0.0002

size $m = 4800$, $M_m = 240$, $C = 40$ and $t \in [-2, 2]$. For the second and fourth panels, we consider $m = 1024$, $M_m = 32$, $C = 20$ and $t \in [-1, 1]$.

Figs. 11 and 12 aim to describe the sensitivity of our test to the sample size. Indeed we consider less image data for the variance estimate $\widehat{\sigma}^{(1)}_{n,m}(t)$ (see second and fourth plots of Fig. 11) and an image of smaller size for $\widehat{\sigma}^{(2)}_{M_m,m}(t)$ (see second and fourth plots of Fig. 12). Specific values of the considered sample sizes are given in the legends of Figs. 11–12. The considered smaller sizes force us to restrain the study to threshold levels that are in the neighborhood of 0. This would ensure that one can find observations of the excursion set. For this reason, in the second and fourth plots of Figs. 11 and 12, we only consider $t \in [-1, 1]$.

In all previous numerical studies of the present section, we fixed the angle $\theta = 0$. We now explore the robustness of our pixel isotropy test with respect to the choice of angle θ in the considered Gaussian covariance model in (12) with $C = 40$. To this aim, we evaluate on $n = 2000$ images of size $m = 512$, the $\widehat{p}_{\text{value}}$ with $\widehat{\sigma}^2_m(t) = \widehat{\sigma}^{(1)}_{n,m}(t)$ under H_1 with $b = 1.5$ for several values of angle $\theta = \pi/12, \pi/8, \pi/6$ and $\pi/3$. The largest $p-$ value obtained in this numerical study is smaller then 10^{-3}. These results can be compared with the similar performances obtained in Fig. 11 for $\theta = 0$ (third and fourth panels).

However, notice that we only test a form of isotropy with respect to the preferential axis (e_1, e_2). Obviously, there exist anisotropic models where $\rho(e_1) = \rho(e_2)$. This is the case of our Gaussian affine model in (12) when considering $\theta = \pi/4$. In Fig. 13 we see how in this case, the proposed test accepts the pixel isotropy ($\rho(e_1) = \rho(e_2)$) but is unable to detect the global anisotropy of the underlying random field.

To end this numerical studies section, in we present the $\widehat{p}_{\text{value}}$ of the test with $\widehat{\sigma}^2_m(t) = \widehat{\sigma}^{(1)}_{n,m}(t)$ by considering $n = 2000$ images of size $m = 512$, for critical values of $b = 1.1$ and $b = 1.2$, $C = 40$ and several levels in $t \in [-2, 2]$. Unsurprisingly, the ability of the test to detect anisotropy for critical values of parameter b, decreases for extreme thresholds t.

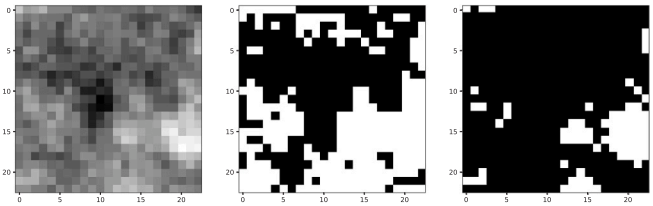

Fig. 14. A realization pixels image with $m = 24$ from a Gaussian random field with covariance $\rho(x) = e^{-\kappa\|x\|^2}$ with $\kappa = 0.25$ (left panel) and the associated thresholded images for $t = 0$ (center panel) and $t = 1$ (right panel).

5. Comparative study

This section is devoted to a comparative study with Guan et al. (2004). This purely nonparametric method is based on the estimation of the semivariogram γ of the random field X, *i.e* $\gamma(h) = \mathrm{Var}\left(X_{s+h} - X_s\right)$, for $h, s \in \mathbb{R}^2$. The main idea is that, under the isotropy hypothesis, the values of γ at any two spatial lags h_1 and h_2 that have the same norm are equal, regardless of the direction of the lags.

The isotropy test in Guan et al. (2004) involves the estimation of the semivariogram, γ, on a finite set of chosen lags. Then they establish a central limit theorem when the domain increases and under moment and mixing conditions on the random field. The simulation for Guan et al. (2004) are provided using the function `GuanTestGrid` from the R `package spTest` (see Weller (2018)). Since this method is based on the estimation of the complete covariance matrix, it implies a high computational cost. For this reason the considered simulation study is limited to $m = 24$ size images. For the Guan et al. (2004)'s method we display the approximate finite-sample adjusted p_{value} computed by using the sub-blocks created by the moving windows (see Guan et al. (2004), Section 3.3 for details).

In Fig. 14 (left panel) we draw a realization of a Gaussian random field with exponential covariance with covariance $\rho(x) = e^{-\kappa\|x\|^2}$ for $\kappa = 0.25$ and $m = 24$ size image. We also represented two excursion sets (Fig. 14, center and right panels). We chose to apply the perimeter based isotropy test for two different threshold levels: $t = 0$ and $t = 1$. The threshold level $t = 0$ is one that maximizes the mean and minimizes the variance of the perimeter (see Figs. 8 and 10), which makes it the perfect candidate for our inference procedure. However, since we do not necessarily have access to the value of the mean of the whole field, we also present the result of the test for another threshold level, $t = 1$.

We study the distribution of the p_{value} for both methods for two thresholds ($t = 0$ and $t = 1$). The $\widehat{p}_{\text{value}}$ of our perimeter method are estimated by using the estimator of the variance $\widehat{\sigma}^{(1)}_{n,24}(t)$, with $n = 100$. The proportion of $\widehat{p}_{\text{value}}$ below the confidence level 0.05 using the estimation of the semivariogram (Guan et al., 2004) and our pixel isotropy test for both the considered thresholds ($t = 0$ and $t = 1$) is 5%.

In practice, the core of our statistical methodology is based on the *local counting algorithm* that operates just counting the number of transitions between black and white pixels in the thresholded image. As the algorithm accumulates information locally, our method is highly amenable and efficient to the treatment of large data-sets. Conversely, the Guan et al. (2004)'s method requires the estimation of the semivariogram function and the whole covariance function of the random field, besides to establish the statistic test it is required to proceed to a matrix inversion. This approach is significantly more computationally demanding and, thus, less suitable for the analysis of high-resolution images.

6. Pixel isotropy test on bone X-rays

6.1. Description of the considered bone X-rays

The studied X-ray images were acquired at INSERM U658 (Orleans, France) using a standardized procedure (Lespessailles et al., 2007, 2008). They were obtained on the calcaneus (a heel bone) with a direct digital X-ray prototype (BMA$^{\text{TM}}$, D3 A Medical Systems, Orleans, France) with focal distance 1.15 m and X-ray parameters 55 kV and 20 mAs. The high-resolution digital detector integrated into the device prototype had a 50 μm pixel size, providing a spatial resolution of 8 line pairs per millimeter at 10% modulation transfer function. For each subject, the software device selected a region of interest (ROI) of constant size 1.6×1.6 cm^2 (400×400 pixels) corresponding at a same position using three predefined anatomical landmarks localized by the operator (see Fig. 15). The database contains radiographs of 211 post-menopausal women, it was previously studied in Biermé et al. (2009).

We first applied a pre-processing step in order to get stationary images. This step is performed by subtracting the trend which is represented by a plane obtained via a mean-square linear regression. Furthermore, to avoid boundaries issues, we decided to crop from a 400×400 image to a 380×380 image. It is also necessary to standardize the images to be in the centered and unit variance framework, considered in this work.

To insure that the images of two excursion sets can be compared, we chose to select the threshold as quantile levels of the image. Thus for an image X, for $\alpha \in (0, 1)$ the considered threshold is $t_\alpha = \widehat{F}_X^{-1}(\alpha)$ with $\widehat{F}_X$ the empirical cumulative distribution function of the image X. After this pre-processing, Fig. 2 suggested the existence of two clusters in regard to the ratio of the two directional perimeters. Indeed, we observe a cluster of points (i.e., a set of images) for which the ratio $\mathcal{P}_1(t_\alpha)/\mathcal{P}_2(t_\alpha)$ is less than one. Since

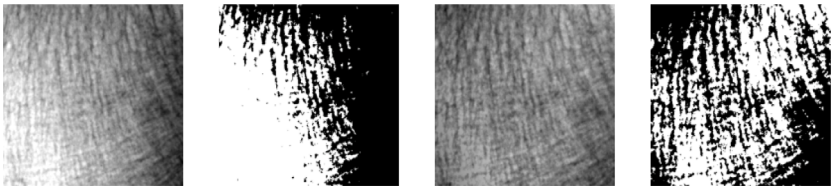

Fig. 15. Example of two images before (first panel) and after (third panel) the stationary procedure and their excursion sets at quantile level $\alpha = 0.5$ (second and four panels).

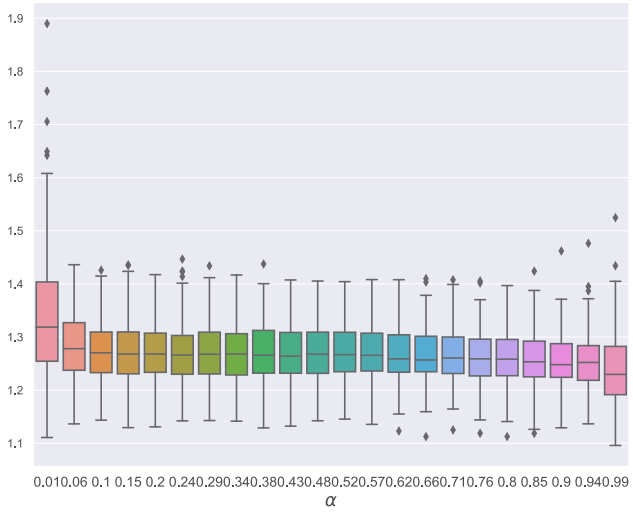

Fig. 16. Boxplots of $(R_{m,i}(t_\alpha))_{i\leq 211}$, with $R_{m,i}(t_\alpha) = \mathcal{P}^{(1)}_{m,i}(t_\alpha)/\mathcal{P}^{(2)}_{m,i}(t_\alpha)$ at quantile t_α level with $t_\alpha = \widehat{F}^{-1}_X(\alpha)$ and $\alpha \in [0.01, 0.99]$. Considered images: stationary thresholded and eventually rotated images of bone X-rays.

the bone's orientation was fixed across images, using three predefined anatomical landmarks, a deep investigation shows that the corresponding images are misoriented. Thus, before proceeding further with the pixel isotropy test, we apply a second pre-processing step: a $\pi/2$-rotation to these specific images. The new obtained boxplots are gathered in Fig. 16.

Furthermore, in order to evaluate the pixel level of correlation in the considered images, we estimate $\rho(e_j)$ by applying Corollary 3.2 and using the total variation of the image for $j = 1, 2$. Fig. 17 confirms the highly pixel dependence behavior of the considered images, *i.e* $\widehat{\rho}_i(e_j) \approx 1$ for $j = 1, 2$ and $1 \leq i \leq 211$. As already remarked in the introduction, since these bone X-rays images have highly local pixel dependence (see the estimated $\widehat{\rho}_i(e_1)$ and $\widehat{\rho}_i(e_2)$, for $i \leq 211$ in previous Fig. 17) the ratio of the two directional perimeters is expected to be invariant with respect to the threshold (see Proposition 3.1, Eqs. (3) and (5), for mathematical details). This stable behavior in terms of t_α, for $\alpha \in [0.01, 0.99]$, is evident in the boxplots of Fig. 16.

6.2. Applying the pixel isotropy test

We can now proceed to the pixel isotropy test. We consider the bone X-rays images, stationary thresholded with different quantile levels t_α, for $\alpha \in [0.01, 0.99]$ and eventually rotated. We compute $p_{\text{value},i}(t_\alpha) = 2\mathbb{P}\left(\mathcal{N}(0,1) > \left|R_i(t_\alpha) - 1\right| / \widehat{\sigma}^{(1)}_{211,380}(t_\alpha)\right)$, for each image X_i with the Monte Carlo estimated variance $\widehat{\sigma}^{(1)}_{211,380}(t_\alpha)$. Then we evaluate $\widehat{p}_{\text{value},211}(t_\alpha) = \frac{1}{211}\sum_{i=1}^{211} p_{\text{value},i}(t_\alpha)$, for any considered threshold t_α. As expected, the result of the hypothesis test gives us $\widehat{p}_{\text{value}}(t_\alpha) < 0.05$, for any t_α, which indicates that the data clearly exhibit anisotropy. Moreover, our test rejects here $H_0 : \rho(e_1) = \rho(e_2)$, i.e., the invariance in distribution under a rotation of angle $\pi/2$.

7. Conclusion and discussion

In this paper, we introduced a novel statistical technique for evaluating the pixel isotropy property of a stationary discrete Gaussian random field. By utilizing the directional perimeter of the excursion set, we are able to build a consistent test only based on this sparse observation. We also successfully applied the test to real world data to test the anisotropic nature of bone texture. As we have seen above, the proposed test does not require any prior knowledge on the covariance function of the underlying field. However, unsurprisingly, it performs better when the selected threshold is close to the mean value of the field and worse for extreme threshold levels.

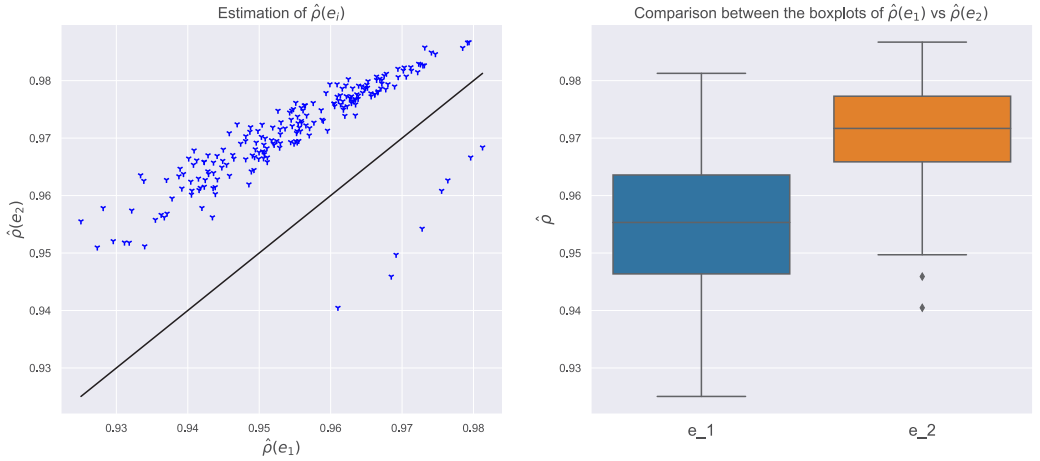

Fig. 17. Left panel: $\left(\widehat{\rho}_i(e_1), \widehat{\rho}_i(e_2)\right)$ for each image X_i. Right panel: boxplot of $(\widehat{\rho}_i(e_1))_{i\leq 211}$ (blue) and $(\widehat{\rho}_i(e_2))_{i\leq 211}$ (orange). (For interpretation of the references to color in this figure legend, the reader is referred to the web version of this article.)

As previously remarked, we can have an anisotropic image with equal horizontal and vertical contributions of the perimeter (see, for example, Fig. 13 for an illustration of this drawback). However, one could adapt results in the present paper by applying a rotation over a direction to the image, and then implement the test to verify if the field is anisotropic in regard to that particular direction. Another potential improvement would be to study the behavior of the ratio between the first and second moments of the directional perimeter for extreme thresholds. If an equivalence between the two is established, it would short-cut the inference of the variance, using the first moment instead, and hopefully increasing the performance of the test for extreme thresholds. Finally, we obtained a closed form for both the first and second moments which renders possible a thorough study of the *infill* framework (*i.e.* $\rho(e_i) \to 1$), which yields a shift from the discrete setting to the continuous one.

Acknowledgments

The authors would like to express their sincere gratitude to two anonymous referees and the Associate Editor for their valuable comments and remarks, which have considerably improved this work. The authors gratefully acknowledge the French government, through the project ANR MISTIC (ANR-19-CE40-0005) and the 3IA Côte d'Azur Investments in the Future project managed by the National Research Agency (ANR) with the reference number ANR-19-P3IA-0002.

Appendix A. Lemmas concerning the two-, three- and four-cells configurations

Lemma A.1 (*Computation of the Four-cells Contribution*). *Let $j \in \{1,2\}$ and let $x \in \mathbb{Z}^2$ such that the covariance matrix of the Gaussian vector $\left(X_0, X_{e_1}, X_x, X_{x+e_j}\right)$ is invertible. Let us define the following coefficients,*

$$\Delta\rho(x) = \rho(x-e_1) - \rho(x) \text{ and } S\rho(x) = \rho(x-e_1) + \rho(x).$$

Then, $\sigma_1^{(-)} > 0$, $\sigma_1^{(+)} > 0$, $\pi_W^{(-,j)}(x) > 0$ and $\pi_Z^{(+,j)}(x) > 0$, where we have introduced the following quantities,

$$\begin{cases} \sigma_1^{(-)} &= \sqrt{2(1-\rho(e_1))} \\ \sigma_1^{(+)} &= \sqrt{2(1+\rho(e_1))} \end{cases}$$

$$\begin{cases} \pi_U^{(-,j)}(x) &= \frac{1}{\sigma_1^{(-)}}\left(\Delta\rho(x+e_j) - \Delta\rho(x)\right) \\ \pi_V^{(-,j)}(x) &= \frac{1}{\sigma_1^{(+)}}\left(S\rho(x+e_j) - S\rho(x)\right) \\ \pi_W^{(-,j)}(x) &= \left(2(1-\rho(e_j)) - \pi_U^{(-,j)}(x)^2 - \pi_V^{(-,j)}(x)^2\right)^{1/2} \end{cases}$$

$$\begin{cases} \pi_U^{(+,j)}(x) &= \frac{1}{\sigma_1^{(-)}}\left(\Delta\rho(x) + \Delta\rho(x+e_j)\right) \\ \pi_V^{(+,j)}(x) &= \frac{1}{\sigma_1^{(+)}}\left(S\rho(x) + S\rho(x+e_j)\right) \\ \pi_W^{(+,j)}(x) &= \frac{-1}{\pi_W^{(-,j)}(x)}\left(\pi_U^{(-,j)}(x)\pi_U^{(+,j)}(x) + \pi_V^{(-,j)}(x)\pi_V^{(+,j)}(x)\right) \\ \pi_Z^{(+,j)}(x) &= \left(2(1+\rho(e_j)) - \pi_U^{(+,j)}(x)^2 - \pi_V^{(+,j)}(x)^2 - \pi_W^{(+,j)}(x)^2\right)^{1/2}. \end{cases}$$

Moreover,

$$\begin{aligned}
&\mathbb{E}\big(f_t^{(1)}(0)f_s^{(j)}(x)\big)\\
&=\mathbb{E}\left(\mathbb{1}_{\left\{|2t-\sigma_1^{(+)}V|\le\sigma_1^{(-)}|U|\right\}}\right.\\
&\left|\Phi_{\pi_Z^{(+,j)}(x)}\Big(2s-\frac{2\Delta\rho(x)}{\sigma_1^{(-)}}U-\frac{2S\rho(x)}{\sigma_1^{(+)}}V+\Big(\pi_W^{(-,j)}(x)-\pi_W^{(+,j)}(x)\Big)W\Big)\right.\\
&\left.\left.-\Phi_{\pi_Z^{(+,j)}(x)}\Big(2s-\frac{2\Delta\rho(x+e_j)}{\sigma_1^{(-)}}U-\frac{2S\rho(x+e_j)}{\sigma_1^{(+)}}V-\Big(\pi_W^{(+,j)}(x)+\pi_W^{(-,j)}(x)\Big)W\Big)\right|\right)
\end{aligned}\tag{A.1}$$

with Φ_α the $\mathcal{N}(0,\alpha^2)$-cumulative distribution function and $(U,V,W)\sim\mathcal{N}(0,I_3)$.

Proof. Recall that we have introduced $\Delta_x^{(j)}$ and $S_x^{(j)}$ in (11). The covariance matrix of the Gaussian vector $\left(\Delta_0^{(1)},S_0^{(1)},\Delta_x^{(j)},S_x^{(j)}\right)$ is equal to $\Sigma_j(x)=\begin{pmatrix}A_1 & B_j(x)\\ B_j^T(x) & A_j\end{pmatrix}$ with $A_j=\begin{pmatrix}2(1-\rho(e_j)) & 0\\ 0 & 2(1+\rho(e_j))\end{pmatrix}$ and $B_j(x)=\begin{pmatrix}\Delta\rho(x+e_j)-\Delta\rho(x) & \Delta\rho(x)+\Delta\rho(x+e_j)\\ S\rho(x+e_j)-S\rho(x) & S\rho(x)+S\rho(x+e_j)\end{pmatrix}$.

By assumption, $\Sigma_j(x)$ is invertible, thus, applying the Cholesky decomposition yields the existence of an invertible lower triangular matrix $L(x)$ such that $\Sigma_j(x)=L(x)L(x)^T$. The matrix $L(x)$ is given by

$$L(x)=\begin{pmatrix}\sigma_1^{(-)} & 0 & 0 & 0\\ 0 & \sigma_1^{(+)} & 0 & 0\\ \pi_U^{(-,j)}(x) & \pi_V^{(-,j)}(x) & \pi_W^{(-,j)}(x) & 0\\ \pi_U^{(+,j)}(x) & \pi_V^{(+,j)}(x) & \pi_W^{(+,j)}(x) & \pi_Z^{(+,j)}(x)\end{pmatrix}$$

with the coefficients introduced in the statement of the lemma. Furthermore, $\det(L(x))\neq 0$ implies that $\sigma_1^{(\pm)}\neq 0$, $\pi_W^{(-,j)}(x)\neq 0$ and $\pi_Z^{(+,j)}(x)\neq 0$ as stated in the quoted lemma. This decomposition allows us to write $\begin{pmatrix}\Delta_0^{(1)}\\ S_0^{(1)}\\ \Delta_x^{(j)}\\ S_x^{(j)}\end{pmatrix}=L(x)\begin{pmatrix}U\\ V\\ W\\ Z\end{pmatrix}$, with $(U,V,W,Z)\sim\mathcal{N}\left(0,I_4\right)$. Developing the indicator functions that appear in Lemma 3.7, we get the following expression

$$\begin{aligned}
&\mathbb{E}\left(f_t^{(1)}(0)f_s^{(j)}(x)\right)\\
&=\mathbb{E}\left(\mathbb{1}_{\left\{|2t-S_0^{(1)}|\le|\Delta_0^{(1)}|\right\}}\mathbb{1}_{\left\{|2s-S_x^{(j)}|\le|\Delta_x^{(j)}|\right\}}\right)\\
&=\mathbb{E}\left(\mathbb{1}_{\left\{|2t-S_0^{(1)}|\le|\Delta_0^{(1)}|\right\}}\mathbb{1}_{\left\{2s-\pi_U^{(+,j)}(x)U-\pi_V^{(+,j)}(x)V-\pi_W^{(+,j)}(x)W-|\Delta_x^{(j)}|\le\pi_Z^{(+,j)}(x)Z\right.}\right.\\
&\qquad\left.\left.\le 2s-\pi_U^{(+,j)}(x)U-\pi_V^{(+,j)}(x)V-\pi_W^{(+,j)}(x)W+|\Delta_x^{(j)}|\right\}\right).
\end{aligned}$$

The variable $\pi_Z^{(+,j)}Z$ being distributed as $\mathcal{N}\left(0,\pi_Z^{(+,j)}(x)^2\right)$ and $\Phi_{\pi_Z^{(+,j)}(x)}$ being an increasing function, we get

$$\begin{aligned}
&\mathbb{E}\big(f_t^{(1)}(0)f_s^{(j)}(x)\big)\\
&=\mathbb{E}\left(\mathbb{1}_{\left\{|2t-\sigma_1^{(+)}V|\le\sigma_1^{(-)}|U|\right\}}\right.\\
&\left|\Phi_{\pi_Z^{(+,j)}(x)}\left(2s-\pi_U^{(+,j)}(x)U-\pi_V^{(+,j)}(x)V-\pi_W^{(+,j)}(x)W+\Delta_x^{(j)}\right)\right.\\
&\left.\left.-\Phi_{\pi_Z^{(+,j)}(x)}\left(2s-\pi_U^{(+,j)}(x)U-\pi_V^{(+,j)}(x)V-\pi_W^{(+,j)}(x)W-\Delta_x^{(j)}\right)\right|\right),
\end{aligned}$$

which directly gives (A.1). □

Lemma A.2 (*Computation of the Three-cells Contribution*). *Let $j\in\{1,2\}$ and let us assume that the covariance matrix of the Gaussian vector $(X_0,X_{e_1},X_{e_1+e_j})$ is invertible. Then, considering the coefficients $\sigma_1^{(-)}$ $\sigma_1^{(+)},\pi_U^{(-,j)}(e_1),\pi_V^{(-,j)}(e_1),\pi_W^{(-,j)}(e_1)$ that are defined in Lemma A.1, we have $\sigma_1^{(-)}>0$, $\sigma_1^{(+)}>0$, $\pi_W^{(-,j)}(e_1)>0$, and*

$$\begin{aligned}
&\mathbb{E}\big(f_t^{(1)}(0)f_s^{(j)}(e_1)\big)\\
&=\mathbb{E}\left(\mathbb{1}_{\left\{\left|2t-\sigma_1^{(+)}V\right|\le\left|\sigma_1^{(-)}U\right|\right\}}\mathbb{1}_{\left\{\sigma_1^{(-)}U+\sigma_1^{(+)}V\le 2s\right\}}\right.\\
&\left.\left(1-\Phi_{\pi_W^{(-,j)}(e_1)}\Big(s-(\frac{1}{2}\sigma_1^{(-)}+\pi_U^{(-,j)}(e_1))U-(\frac{1}{2}\sigma_1^{(+)}+\pi_V^{(-,j)}(e_1))V\Big)\right)\right)
\end{aligned}$$

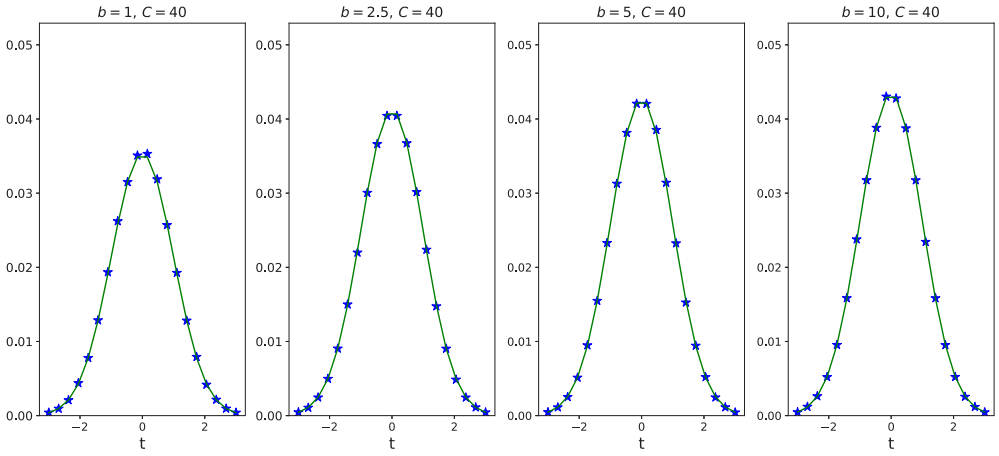

Fig. A.18. Values of $\mathbb{E}\big(f_t^{(1)}(0) f_t^{(2)}(e_1)\big)$ for different values of b and $C = 40$. Theoretical expectation in full green lines, associated empirical values in green. Here $\text{MC}_{\text{INT}} = 1\,000\,000$ and $n = 1\,000\,000$.

$$+\ \mathbb{E}\left(\mathbb{1}_{\left\{\left|2t-\sigma_1^{(+)}V\right|\le\left|\sigma_1^{(-)}U\right|\right\}}\mathbb{1}_{\left\{\sigma_1^{(-)}U+\sigma_1^{(+)}V\ge 2s\right\}}\right.$$
$$\left.\boldsymbol{\Phi}_{\pi_W^{(-,j)}(e_1)}\Big(s-(\frac{1}{2}\sigma_1^{(-)}+\pi_U^{(-,j)}(e_1))\,U-(\frac{1}{2}\sigma_1^{(+)}+\pi_V^{(-,j)}(e_1))\,V\Big)\right), \tag{A.2}$$

where $\boldsymbol{\Phi}_\alpha$ stands for the $\mathcal{N}(0,\alpha^2)$-cumulative distribution function and $(U,V)\sim\mathcal{N}(0,I_2)$.

Proof. Following a similar method as for the proof of Lemma A.1, we consider the transformed vector $\left(\Delta_0^{(1)}, S_0^{(1)}, \Delta_{e_1}^{(j)}\right)$. Its covariance matrix is invertible by assumption and its Cholesky decomposition allows us to write $\begin{pmatrix}\Delta_0^{(1)}\\ S_0^{(1)}\\ \Delta_{e_1}^{(j)}\end{pmatrix} = K(e_1)\begin{pmatrix}U\\V\\W\end{pmatrix}$, with $(U,V,W)\sim\mathcal{N}\left(0,I_3\right)$ and

$$K(e_1)=\begin{pmatrix}\sigma_1^{(-)} & 0 & 0\\ 0 & \sigma_1^{(+)} & 0\\ \pi_U^{(-,j)}(e_1) & \pi_V^{(-,j)}(e_1) & \pi_W^{(-,j)}(e_1)\end{pmatrix}$$

Then, thanks to the three-cells case of Lemma 3.7, we have

$$\mathbb{E}\big(f_t^{(1)}(0)\, f_s^{(j)}(e_1)\big)=\mathbb{E}\left(\mathbb{1}_{\left\{|2t-S_0^{(1)}|\le|\Delta_0^{(1)}|\right\}}\mathbb{1}_{\left\{|2s-(S_0^{(1)}+\Delta_0^{(1)}+\Delta_{e_1}^{(j)})|\le|\Delta_{e_1}^{(j)}|\right\}}\right),$$

where we can use the vector (U,V,W) to write the first indicator function as

$$\mathbb{1}_{\left\{|2s-S_0^{(1)}|\le|\Delta_0^{(1)}|\right\}}=\mathbb{1}_{\left\{|2s-\sigma_1^{(+)}V|\le|\sigma_1^{(-)}U|\right\}},$$

and to split the second indicator function as

$$\begin{aligned}\mathbb{1}_{\left\{|2s-S_x^{(j)}|\le|\Delta_x^{(j)}|\right\}}=&\ \mathbb{1}_{\left\{\sigma_1^{(-)}U+\sigma_1^{(+)}V\le 2s\right\}}\\ &\mathbb{1}_{\left\{\pi_W^{(-,j)}(e_1)W\ge\left(s-\left(\frac{1}{2}\sigma_1^{(-)}+\pi_U^{(-,j)}(e_1)\right)U-\left(\frac{1}{2}\sigma_1^{(+)}+\pi_V^{(-,j)}(e_1)\right)V\right)\right\}}\\ &+\ \mathbb{1}_{\left\{\sigma_1^{(-)}U+\sigma_1^{(+)}V\ge 2s\right\}}\\ &\mathbb{1}_{\left\{\pi_W^{(-,j)}(e_1)W\le\left(s-\left(\frac{1}{2}\sigma_1^{(-)}+\pi_U^{(-,j)}(e_1)\right)U-\left(\frac{1}{2}\sigma_1^{(+)}+\pi_V^{(-,j)}(e_1)\right)V\right)\right\}}.\end{aligned}$$

Putting everything together yields Eq. (A.2). □

Fig. A.18 is a numerical illustration of Eq. (A.2) and it validates the obtained theoretical result. The empirical values in Figs. A.18 are computed by simulating Gaussian vectors of dimension 3 with the proper covariance structure and computing the expectation of the indicator function directly.

Applying the same strategy as above, we obtain the following lemma.

Lemma A.3 (*Computation of the Two Cells Contribution*). *Assuming that* $|\rho(e_1)| \neq 1$, *it holds that*

$$\mathbb{E}\big(f_t^{(1)}(0)f_s^{(1)}(0)\big) = \mathbb{E}\left(\mathbb{1}_{\left\{|s-t|\leq|Z|\sqrt{2(1-\rho(e_1))}\right\}} \left(\Phi\Big(\frac{\sqrt{2}\max(t,s)+\sqrt{1-\rho(e_1)}|Z|}{\sqrt{1+\rho(e_1)}}\Big) - \Phi\Big(\frac{\sqrt{2}\min(t,s)-\sqrt{1-\rho(e_1)}|Z|}{\sqrt{1+\rho(e_1)}}\Big)\right)\right),$$

where $Z \sim \mathcal{N}(0,1)$.

We develop now computations for covariances.

Lemma A.4. *Let* $s,t \in \mathbb{R}$. *We have*

$$\mathrm{Cov}\left(\mathcal{P}_m(t),\mathcal{P}_m(s)\right) = \sum_{1\leq i,j\leq 2} \mathrm{Cov}(\mathcal{P}_m^{(i)}(t),\mathcal{P}_m^{(j)}(s)), \tag{A.3}$$

with, for $x=(x_1,x_2)\in\mathbb{Z}^2$,

$$\mathrm{Cov}\left(\mathcal{P}_m^{(1)}(t),\mathcal{P}_m^{(1)}(s)\right) = \sum_{x_2=(1-m)}^{m-1}\sum_{x_1=(2-m)}^{m-2}\left(m-|x_2|\right)\left(m-1-|x_1|\right)\mathrm{Cov}\left(f_t^{(1)}(0),f_s^{(1)}(x)\right),$$

$$\mathrm{Cov}\left(\mathcal{P}_m^{(2)}(t),\mathcal{P}_m^{(2)}(s)\right) = \sum_{x_1=(1-m)}^{m-1}\sum_{x_2=(2-m)}^{m-2}\left(m-|x_1|\right)\left(m-1-|x_2|\right)\mathrm{Cov}\left(f_t^{(2)}(0),f_s^{(2)}(x)\right),$$

and finally,

$$\mathrm{Cov}\left(\mathcal{P}_m^{(1)}(t),\mathcal{P}_m^{(2)}(s)\right) = \sum_{x_1=2-m}^{m-1}\sum_{x_2=1-m}^{m-2}\left(m-|x_1|-\mathbb{1}_{x_1\leq 0}\right)\left(m-|x_2|-\mathbb{1}_{\{x_2\geq 0\}}\right)\mathrm{Cov}\left(f_t^{(1)}(0),f_s^{(2)}(x)\right).$$

Proof. Let us start with the computation of $\mathrm{Cov}(\mathcal{P}_m^{(1)}(t),\mathcal{P}_m^{(1)}(s))$. By stationarity, we have

$$\mathrm{Cov}(\mathcal{P}_m^{(1)}(t),\mathcal{P}_m^{(1)}(s)) = \sum_{x\in\mathbb{G}_m^{(1)}}\sum_{y\in\mathbb{G}_m^{(1)}}\mathrm{Cov}\left(f_t^{(1)}(0),f_s^{(1)}(y-x)\right).$$

For $z_1 = y_1 - x_1$ one has

$$\begin{cases}0\leq x_1\leq m-2\\ 0\leq y_1\leq m-2\end{cases} \Leftrightarrow \begin{cases}2-m\leq z_1\leq m-2\\ \max(0,-z_1)\leq x_1\leq \min(m-2,m-2-z_1)\end{cases},$$

and similarly for $z_2 = y_2 - x_2$

$$\begin{cases}0\leq x_2\leq m-1\\ 0\leq y_2\leq m-1\end{cases} \Leftrightarrow \begin{cases}1-m\leq z_2\leq m-1\\ \max(0,-z_2)\leq x_2\leq \min(m-1,m-1-z_2)\end{cases}.$$

Thus,

$$\mathrm{Cov}\left(\mathcal{P}_m^{(1)}(t),\mathcal{P}_m^{(1)}(s)\right) = \sum_{z_1=(2-m)}^{m-2}\sum_{z_2=(1-m)}^{m-1}\left(m-1-|z_1|\right)\left(m-|z_2|\right)\mathrm{Cov}\left(f_t^{(1)}(0),f_s^{(1)}(z)\right).$$

For $\mathrm{Cov}\left(\mathcal{P}_m^{(1)}(t),\mathcal{P}_m^{(2)}(s)\right)$, we still have by stationarity

$$\mathrm{Cov}\left(\mathcal{P}_m^{(1)}(t),\mathcal{P}_m^{(2)}(s)\right) = \sum_{x\in\mathbb{G}_m^{(1)}}\sum_{y\in\mathbb{G}_m^{(2)}}\mathrm{Cov}\left(f_t^{(1)}(0),f_s^{(2)}(y-x)\right),$$

and again, considering $z_1 = y_1 - x_1$ and $z_2 = y_2 - x_2$, we get

$$\mathrm{Cov}\left(\mathcal{P}_m^{(1)}(t),\mathcal{P}_m^{(2)}(s)\right) = \sum_{z_1=2-m}^{m-1}\sum_{z_2=1-m}^{m-2}\left(m-|z_1|-\mathbb{1}_{z_1\leq 0}\right)\left(m-|z_2|-\mathbb{1}_{z_2\geq 0}\right)\mathrm{Cov}\left(f_t^{(1)}(0),f_s^{(2)}(z)\right). \quad \square$$

Appendix B. Proofs

Proof of Proposition 3.1. Applying the stationarity hypothesis yields the first assertion.

The integral expression of $h(t,\cdot)$ in (3) can be derived from the formula in Proposition 16.1.1 in Lantuéjoul (2002) through a change of variable that is explicitly written at the end of the proof of this proposition.

Let us assume that $|\rho(e_i)| \neq 1$. In order to get the second expression (4), considering Formula (10) for $f_t^{(i)}(0)$, one can write that,

$$\mathbb{E}\big(f_t^{(i)}(0)\big) = \mathbb{E}\big(\mathbb{1}_{\left\{\left|2t-S_0^{(i)}\right|\leq\left|\Delta_0^{(i)}\right|\right\}}\big),$$

where we recall the notation $\Delta_0^{(i)} := X_{e_i} - X_0$ and $S_0^{(i)} := X_{e_i} + X_0$. The covariance matrix of the Gaussian vector $\left(\Delta_0^{(i)}, S_0^{(i)}\right)$ is given by

$$\widetilde{\Sigma}_i(0) = \begin{pmatrix} 2(1-\rho(e_i)) & 0 \\ 0 & 2(1+\rho(e_i)) \end{pmatrix},$$

which directly implies that the two variables $\Delta_0^{(i)}$ and $S_0^{(i)}$ are independent. Hence, we can write

$$\Delta_0^{(i)} = \sqrt{2(1-\rho(e_i))}U \text{ and } S_0^{(i)} = \sqrt{2(1+\rho(e_i))}V \text{ with } (U,V) \sim \mathcal{N}\left(0, I_2\right),$$

and so we get

$$\begin{aligned}
\mathbb{E}\big(f_t^{(i)}(0)\big) &= \mathbb{E}\left(\mathbb{1}_{\left\{\left|2t-S_0^{(i)}\right|\leq\left|\Delta_0^{(i)}\right|\right\}}\right) \\
&= \mathbb{E}\left(\mathbb{1}_{\left\{\frac{2t-\sqrt{2(1-\rho(e_i))}|U|}{\sqrt{2(1+\rho(e_i))}} \leq V \leq \frac{2t+\sqrt{2(1-\rho(e_i))}|U|}{\sqrt{2(1+\rho(e_i))}}\right\}}\right) \\
&= \mathbb{E}\left(\Phi\Big(\frac{\sqrt{2}t + \sqrt{1-\rho(e_i)}\,|U|}{\sqrt{1+\rho(e_i)}}\Big) - \Phi\Big(\frac{\sqrt{2}t - \sqrt{1-\rho(e_i)}\,|U|}{\sqrt{1+\rho(e_i)}}\Big)\right) \\
&= h(t,\rho(e_i)),
\end{aligned}$$

with function $h(t,\cdot)$ exactly as in (4). □

Proof of Theorem 3.4. This proof is based on a convergence theorem formulated by Arcones (1994). The assumptions $(\mathcal{A}1)$, $(\mathcal{A}2)$ and $(\mathcal{A}3)$ are exactly the ones that are necessary in the cited theorem. They ensure the existence of a finite limit in (6) but no insurance is given concerning the non-degeneracy of the matrix $\Sigma_{2r}^{\star}$. Let us mention that we could have used the formalism of Cayley graphs exposed in Reddy et al. (2018) to get our central limit theorem but it would have required a stronger assumption on the Gaussian field, namely an exponentially decaying covariance function, and no stronger conclusion on the non-degeneracy limit variance would have been obtained.

For the sake of simplicity, we will prove the theorem for one threshold (*i.e.* $r = 1$), the generalized case can be established by following a similar procedure.

Let $t \in \mathbb{R}$. Using the Cramér–Wold method, we will prove that for each $(a_1, a_2) \in \mathbb{R}^2$, we have

$$\frac{a_1}{m}\left(\mathcal{P}_m^{(1)}(t) - \mathbb{E}\left(\mathcal{P}_m^{(1)}(t)\right)\right) + \frac{a_2}{m}\left(\mathcal{P}_m^{(2)}(t) - \mathbb{E}\left(\mathcal{P}_m^{(2)}(t)\right)\right) \xrightarrow[m\to\infty]{d} \mathcal{N}\left(0, \sigma^2(t)\right)$$

with $\sigma^2(t) < \infty$. For $x \in \mathbb{G}_m$, by using the notation introduced in (1), we consider the 3-dimensional Gaussian vector $\mathbb{X}_x = (\mathbb{X}_x^{(i)})_{1\leq i\leq 3} = (X_x, X_{x+e_1}, X_{x+e_2})$ and the function g_t defined on $\mathbb{R}^3$,

$$g_t(u,v,w) := a_1 \mathbb{1}_{\{\min(u,v)<t\leq\max(u,v)\}} + a_2 \mathbb{1}_{\{\min(u,w)<t\leq\max(u,w)\}}.$$

Hence, rewriting the following sum, we get, for $x = (x_1, x_2)$,

$$\sum_{x\in\mathbb{G}_m} g_t\left(\mathbb{X}_x\right) = \sum_{x_1=0}^{m-1}\sum_{x_2=0}^{m-1} g_t\left(\mathbb{X}_{x_1,x_2}\right) = a_1\mathcal{P}_m^{(1)}(t) + a_2\mathcal{P}_m^{(2)}(t) + A_m^{(1)} + A_m^{(2)},$$

where

$$A_m^{(1)} = a_1\sum_{x_2=0}^{m-1} f_t^{(1)}(m-1, x_2) \text{ and } A_m^{(2)} = a_2\sum_{x_1=0}^{m-1} f_t^{(2)}(x_1, m-1).$$

Note that $|g(t)| \leq |a_1| + |a_2|$, thus, $\mathbb{E}\left(g_t\left(\mathbb{X}_{0,0}\right)^2\right) < (|a_1| + |a_2|)^2$. On the one hand, under $(\mathcal{A}1)$, for all $p, q \in \{1,2,3\}$,

$$\lim_{m\to\infty} m^{-2}\sum_{x\in\mathbb{G}_m}\sum_{y\in\mathbb{G}_m}\mathbb{E}\left(\mathbb{X}_x^{(p)}\mathbb{X}_y^{(q)}\right) \text{ exists,}$$

since ρ is the covariance function of X. On the other hand, $(\mathcal{A}3)$ implies that $\sum_{x\in\mathbb{Z}^2}\rho(x)^2 < +\infty$. Indeed, it comes from Fatou's Lemma using the fact that

$$\frac{1}{m^2}\sum_{x,y\in\mathbb{G}_m}\rho(x-y)^2=\sum_{|x_1|<m}\sum_{|x_2|<m}\left(1-\frac{|x_1|}{m}\right)\left(1-\frac{|x_2|}{m}\right)\rho(x)^2.$$

Applying again Fatou's Lemma yields the existence of

$$\lim_{m\to\infty} m^{-2}\sum_{x\in\mathbb{G}_m}\sum_{y\in\mathbb{G}_m}\mathbb{E}\left(\mathbb{X}_x^{(p)}\mathbb{X}_y^{(q)}\right)^2,\quad \forall p,q\in\{1,2,3\}.$$

Hence, we can apply Theorem 2 in Arcones (1994) and get that

$$m^{-1}\sum_{x\in\mathbb{G}_m} g_t\left(\mathbb{X}_x\right)-\mathbb{E}\left(g_t\left(\mathbb{X}_x\right)\right)\xrightarrow[m\to\infty]{d}\mathcal{N}\left(0,\sigma^2(t)\right).$$

Now, it only remains to check that $\frac{1}{m}A_m^{(i)}$ tends to 0 in probability for $i\in\{1,2\}$. Let us verify it for $A_m^{(1)}$. By stationarity, the random variable $A_m^{(1)}$ has the same law as

$$\widetilde{A}_m^{(1)}=\sum_{x_2=0}^{m-1}\widetilde{g}_t(X_{0,x_2},X_{1,x_2}),\quad \text{where } \widetilde{g}_t(u,v)=a_1\mathbb{1}_{\{\min(u,v)<t\le\max(u,v)\}}.$$

Then, Assumptions $(\mathcal{A}2)$ and $(\mathcal{A}3)$ ensure that we can again apply Theorem 2 in Arcones (1994) so that the convergence in distribution of $\left(\frac{1}{m^{1/2}}(\widetilde{A}_m^{(1)}-\mathbb{E}(\widetilde{A}_m^{(1)}))\right)_m$ implies that $\left(\frac{1}{m}(\widetilde{A}_m^{(1)}-\mathbb{E}(\widetilde{A}_m^{(1)}))\right)_m$ tends to 0 in probability. □

Proof of Lemma 3.8. We first recall that since $(X_x)_{x\in\mathbb{Z}^2}$ is stationary, by Böchner–Herglotz theorem, its covariance function may be written as

$$\rho(x)=\int_{\mathbb{T}^2}e^{ix\cdot\xi}d\mu(\xi),\ \text{for } x\in\mathbb{Z}^2,$$

where μ is a non-negative measure, the so-called spectral measure. Here we note the torus $\mathbb{T}=\mathbb{R}/2\pi\mathbb{Z}$ identified with $(0,2\pi]$. For $n\ge1$ and $x_1,\dots,x_n\in\mathbb{Z}^2$ all distinct, the Gaussian vector $(X_{x_1},\dots,X_{x_n})$ is non degenerate if and only if its covariance matrix Σ_n is invertible. So, let $\lambda_1,\dots,\lambda_n\in\mathbb{R}$ be such that $\sum_{j=1}^n\lambda_jX_{x_j}=0$, *a.s.* Then,

$$\begin{aligned}0&=\mathrm{Var}\left(\sum_{j=1}^n\lambda_jX_{x_j}\right)=\sum_{j=1}^n\sum_{k=1}^n\lambda_j\lambda_k\mathrm{Cov}\left(X_{x_j},X_{x_k}\right)\\&=\sum_{j=1}^n\sum_{k=1}^n\lambda_j\lambda_k\mathrm{Cov}\left(X_0,X_{x_k-x_j}\right)=\sum_{j=1}^n\sum_{k=1}^n\lambda_j\lambda_k\rho\left(x_k-x_j\right).\end{aligned}$$

Writing ρ with respect to its spectral measure one has

$$\begin{aligned}0&=\sum_{j=1}^n\sum_{k=1}^n\lambda_j\lambda_k\int_{\mathbb{T}^2}e^{i(x_k-x_j)\cdot\xi}d\mu(\xi)\\&=\int_{\mathbb{T}^2}\sum_{j=1}^n\sum_{k=1}^n\lambda_j\lambda_ke^{i(x_k-x_j)\cdot\xi}d\mu(\xi)\\&=\int_{\mathbb{T}^2}\left(\sum_{k=1}^n\lambda_ke^{ix_k\cdot\xi}\right)\left(\sum_{j=1}^n\lambda_je^{-ix_j\cdot\xi}\right)d\mu(\xi)\\&=\int_{\mathbb{T}^2}\left|\sum_{k=1}^n\lambda_ke^{ix_k\cdot\xi}\right|^2d\mu(\xi).\end{aligned}$$

Now we use the fact that ρ has a spectral density, say $f\ge0$, to get

$$\int_{\mathbb{T}^2}\left|\sum_{k=1}^n\lambda_ke^{ix_k\cdot\xi}\right|^2f(\xi)d\xi=0.$$

Since there exists an open set U in $(0,2\pi]^2$ with positive measure such that $f>0$ on U, then $\forall\xi\in U$, $\left|\sum_{k=1}^n\lambda_ke^{ix_k\cdot\xi}\right|^2=0$. The family of functions $(\xi\mapsto e^{ix_k\cdot\xi})_{1\le k\le n}$ defined on U being linearly independent, it implies that $\lambda_1=\cdots=\lambda_n=0$, which gives the result. □

Proof of Lemma 3.9. Let us begin by reconsidering the coefficients introduced in Lemma A.1, and let us note $\sigma_j^{(-)}=\sqrt{2(1-\rho(e_j))}$ and $\sigma_j^{(+)}=\sqrt{2(1+\rho(e_j))}$.

If $r(x)=0$ then, $\pi_U^{(-,j)}(x)=\pi_U^{(+,j)}(x)=\pi_V^{(-,j)}(x)=\pi_V^{(+,j)}(x)=0$, $\pi_W^{(-,j)}(x)=\sigma_j^{(-)}$ and $\pi_W^{(+,j)}(x)=\sigma_j^{(+)}$, and hence $\mathrm{Cov}\left(f_t^{(1)}(0),f_s^{(j)}(x)\right)=0$.

So, let us assume now that $r(x)\neq0$.

Considering Eq. (4), we get

$$\mathbb{E}\big(f_s^{(j)}(x)\big) = \mathbb{E}\left(\Phi\Big(\frac{2s+\sigma_j^{(-)}|N|}{\sigma_j^{(+)}}\Big) - \Phi\Big(\frac{2s-\sigma_j^{(-)}|N|}{\sigma_j^{(+)}}\Big)\right)$$
$$= \mathbb{E}\left(\left|\Phi\Big(\frac{2s+\sigma_j^{(-)}N}{\sigma_j^{(+)}}\Big) - \Phi\Big(\frac{2s-\sigma_j^{(-)}N}{\sigma_j^{(+)}}\Big)\right|\right),$$

with N any standard Gaussian variable. Then, recalling Eq. (A.1) in Lemma A.1, we are able to write

$$\mathrm{Cov}\left(f_t^{(1)}(0), f_s^{(j)}(x)\right) = \mathbb{E}\left(\mathbb{1}_{\left\{|2t-\sigma_1^{(+)}V|\le|\sigma_1^{(-)}U|\right\}}\right.$$
$$\left(\left|\Phi\Big(\frac{2s+\sigma_j^{(-)}W}{\sigma_j^{(+)}}+R_1(x)\Big) - \Phi\Big(\frac{2s-\sigma_j^{(-)}W}{\sigma_j^{(+)}}+R_2(x)\Big)\right|\right.$$
$$\left.\left. - \left|\Phi\Big(\frac{2s+\sigma_j^{(-)}W}{\sigma_j^{(+)}}\Big) - \Phi\Big(\frac{2s-\sigma_j^{(-)}W}{\sigma_j^{(+)}}\Big)\right|\right)\right),$$

where we have introduced $R_1(x)$ and $R_2(x)$ as follows,

$$R_1(x) = \frac{1}{\pi_Z^{(+,j)}(x)}\Big(2s - \frac{2\Delta\rho(x)}{\sigma_1^{(-)}}U - \frac{2S\rho(x)}{\sigma_1^{(+)}}V + \big(\pi_W^{(-,j)}(x) - \pi_W^{(+,j)}(x)\big)W\Big)$$
$$- \frac{1}{\sigma_j^{(+)}}\Big(2s+\sigma_j^{(-)}W\Big); \tag{B.1}$$

$$R_2(x) = \frac{1}{\pi_Z^{(+,j)}(x)}\Big(2s - \frac{2\Delta\rho(x+e_j)}{\sigma_1^{(-)}}U - \frac{2S\rho(x+e_j)}{\sigma_1^{(+)}}V - \big(\pi_W^{(-,j)}(x) + \pi_W^{(+,j)}(x)\big)W\Big)$$
$$- \frac{1}{\sigma_j^{(+)}}\Big(2s-\sigma_j^{(-)}W\Big). \tag{B.2}$$

Hence,

$$\left|\mathrm{Cov}\left(f_t^{(1)}(0), f_s^{(j)}(x)\right)\right| \le \mathbb{E}\left(\left|\Phi\left(\frac{2s+\sigma_j^{(-)}W}{\sigma_j^{(+)}}+R_1(x)\right) - \Phi\left(\frac{2s+\sigma_j^{(-)}W}{\sigma_j^{(+)}}\right)\right|\right.$$
$$\left. + \left|\Phi\left(\frac{2s-\sigma_j^{(-)}W}{\sigma_j^{(+)}}\right) - \Phi\left(\frac{2s-\sigma_j^{(-)}W}{\sigma_j^{(+)}}+R_2(x)\right)\right|\right)$$
$$\le C\,\mathbb{E}\left(|R_1(x)| + |R_2(x)|\right), \tag{B.3}$$

for some positive constant C, using the Lipschitz property of Φ.

Now, recalling the expressions introduced in Lemma A.1, we obviously get

$$\left|\pi_U^{(\pm,j)}(x)\right| \le C\,r(x), \qquad \left|\pi_V^{(\pm,j)}(x)\right| \le C\,r(x), \tag{B.4}$$

where, from now on, we denote by C a positive constant depending on ρ but not on x that can change from one line to another. Then, subtracting $\sigma_j^{(-)}$ and applying the inequalities in (B.4) we get,

$$\left|\pi_W^{(-,j)}(x) - \sigma_j^{(-)}\right| \le \sigma_j^{(-)}\left|\left(1 - \frac{\pi_U^{(-,j)}(x)^2}{\left(\sigma_j^{(-)}\right)^2} - \frac{\pi_V^{(-,j)}(x)^2}{\left(\sigma_j^{(-)}\right)^2}\right)^{(1/2)} - 1\right|$$
$$\le C\,r(x)^2. \tag{B.5}$$

From (B.4) and (B.5), we also get

$$\left|\pi_W^{(+,j)}(x)\right| = \frac{1}{\pi_W^{(-,j)}(x)}\left|\pi_U^{(-,j)}(x)\pi_U^{(+,j)}(x) + \pi_V^{(-,j)}(x)\pi_V^{(+,j)}(x)\right|$$
$$\le C\,r(x)^2. \tag{B.6}$$

Finally, from (B.4) and (B.6),

$$\left|\pi_Z^{(+,j)}(x) - \sigma_j^{(+)}\right| \le C\,r(x)^2. \tag{B.7}$$

Coming back to (B.1), we can write

$$|R_1(x)| \le 2s\left|\frac{1}{\pi_Z^{(+,j)}(x)} - \frac{1}{\sigma_j^{(+)}}\right| + \frac{2\,|\Delta\rho(x)|\,|U|}{\pi_Z^{(+,j)}(x)\sigma_1^{(-)}} + \frac{2\,|S\rho(x)|\,|V|}{\pi_Z^{(+,j)}(x)\sigma_1^{(+)}}$$

$$+\left|\frac{\pi_W^{(-,j)}(x)}{\pi_Z^{(+,j)}(x)}-\frac{\sigma_j^{(-)}}{\sigma_j^{(+)}}\right||W|+\left|\frac{\pi_W^{(+,j)}(x)}{\pi_Z^{(+,j)}(x)}\right||W|,$$

and putting together the inequalities in (B.4)–(B.7), we get

$$|R_1(x)|\leq C\,r(x)\Big(|U|+|V|+|W|\Big).$$

A similar upperbound can be obtained for $R_2(x)$ starting from (B.2). Inserting it inside Eq. (B.3) gives the result. □

References

Abaach, M., Biermé, H., Di Bernardino, E., 2021. Testing marginal symmetry of digital noise images through the perimeter of excursion sets. Electron. J. Stat. 15 (2), 6429–6460.

Arcones, M.A., 1994. Limit theorems for nonlinear functionals of a stationary Gaussian sequence of vectors. Ann. Probab. 22 (4), 2242–2274.

Berzin, C., 2021. Estimation of local anisotropy based on level sets. Electron. J. Probab. 26, 1–72.

Biermé, H., Desolneux, A., 2021. The effect of discretization on the mean geometry of a 2D random field. Ann. H. Lebesgue 4, 1295–1345.

Biermé, H., Di Bernardino, E., Duval, C., Estrade, A., 2019. Lipschitz–Killing curvatures of excursion sets for two-dimensional random fields. Electron. J. Stat. 13 (1).

Biermé, H., Richard, F., Benhamou, C.L., 2009. Parametric estimation for Gaussian operator scaling random fields and anisotropy analysis of bone radiograph textures. In: Pohl, K. (Ed.), International Conference on Medical Image Computing and Computer Assisted Intervention MICCAI'09. London, France, pp. 13–24.

Bulinski, A., Spodarev, E., Timmermann, F., 2012. Central limit theorems for the excursion set volumes of weakly dependent random fields. Bernoulli 18 (1), 100–118.

Cabaña, E.M., 1987. Affine processes: a test of isotropy based on level sets. SIAM J. Appl. Math. 47 (4), 886–891.

Chappard, C., Brunet-Imbault, B., Lemineur, G., Giraudeau, B., Basillais, A., Harba, R., Benhamou, C.L., 2005. Anisotropy changes in post-menopausal osteoporosis: characterization by a new index applied to trabecular bone radiographic images. Osteoporos. Int. 16, 1193–1202.

Di Bernardino, E., Duval, C., 2022. Statistics for Gaussian random fields with unknown location and scale using Lipschitz–Killing curvatures. Scand. J. Stat. 49, 143–184.

Di Bernardino, E., Estrade, A., León, J.R., 2017. A test of Gaussianity based on the Euler characteristic of excursion sets. Electron. J. Stat. 11 (1), 843–890.

Gray, S., 1971. Local properties of binary images in two dimensions. IEEE Trans. Comput. C-20 (5), 551–561. http://dx.doi.org/10.1109/t-c.1971.223289.

Guan, Y., Sherman, M., Calvin, J., 2004. A nonparametric test for spatial isotropy using subsampling. J. Amer. Statist. Assoc. 99 (467), 810–821.

Lantuéjoul, C., 2002. Geostatistical Simulation: Models and Algorithms. Springer Berlin Heidelberg, Berlin; New York.

Lespessailles, E., Gadois, C., Kousignian, I., Neveu, J.P., Fardellone, P., Kolta, S., Roux, C., Do-Huu, J.P., Benhamou, C.L., 2008. Clinical interest of bone texture analysis in osteoporosis: a case control multicenter study. Osteoporos. Int. 19, 1019–1028.

Lespessailles, E., Gadois, C., Lemineur, G., Do-Huu, J.P., Benhamou, C.L., 2007. Bone texture analysis on direct digital radiographic images: precision study and relationship with bone mineral density at the os calcis. Calcif. Tissue Int. 80, 97–102.

Lindblad, J., 2005. Surface area estimation of digitized 3D objects using weighted local configurations. Image Vis. Comput. 23 (2), 111–122. http://dx.doi.org/10.1016/j.imavis.2004.06.012, Discrete Geometry for Computer Imagery.

Longuet-Higgins, M.S., 1957. The statistical analysis of a random, moving surface. Philos. Trans. R. Soc. Lond. Ser. A 249, 321–387.

MATLAB, 2021. Update 4 (9.9.0.1570001) (R2020b). The MathWorks Inc., Natick, Massachusetts.

Miller, E., 1999. Alternative tilings for Improved Surface Area estimates by local counting algorithms. Comput. Vis. Image Underst. 74 (3), 193–211.

Molina, A., Feito, F.R., 2002. A method for testing anisotropy and quantifying its direction in digital images. Comput. Graph. 26 (5), 771–784.

Reddy, T., Vadlamani, S., Yogeshwaran, D., 2018. Central limit theorem for exponentially quasi-local statistics of spin models on cayley graphs. J. Statist. Phys..

Richard, F., 2016. Some anisotropy indices for the characterization of Brownian textures and their application to breast images. Spat. Statist. 18, 147–162.

Telschow, F., Schwartzman, A., Cheng, D., Pranav, P., 2020. Estimation of expected Euler characteristic curves of nonstationary smooth Gaussian fields. Ann. Statist. 51, 2272–2297.

Wani, I., Arora, S., 2020. Computer-aided diagnosis systems for osteoporosis detection: a comprehensive survey. Med. Biol. Eng. Comput. 58, 1873–1917.

Weller, Z.D., 2018. spTest: An r package implementing nonparametric tests of isotropy. J. Stat. Softw. 83 (4), 1–24.

Weller, Z.D., Hoeting, J.A., 2016. A review of nonparametric hypothesis tests of isotropy properties in spatial data. Statist. Sci. 31 (3), 305–324.

Worsley, K.J., 1996. The geometry of random images. Chance 9 (1), 27–40.